# A First-in-Class Therapy Targeting Transcription-Replication Conflicts Drives Synthetic Lethality in Homologous Recombination Deficient Cancers

Yi Chieh Lim[1,2,9✉], Soak Kuan Lai[3,9], Ru Han Yang[3,9], Yong Kang Chua[3], Rémi Patouret[1], Vaishnervi Manoj[3,4], Colin Chun Xuan Soh[3], Benjamin Lebeau[3], Ning Cham[1], Wei Meng[3], Sze Keong Tey[3,5], Szu Ling Yeap[3], Songjing Zhang[3], Jessie Yong Xing Woon[3,6], Zahin Ali[3,7]. Marek Mutwil[3,8], Pritpal Singh[3], Melissa Jane Fullwood[3], Linda LD Zhong[3], Xue Ming Dong[3], Chiba Shunsuke[1], Cheng Gee Koh[3✉], Hoi Yeung Li[3✉]

[1]School of Chemistry, Chemical Engineering and Biotechnology, Nanyang Technological University, Singapore
[2]Nanyang Biologics Pte Ltd, Singapore
[3]School of Biological Sciences, College of Science, Nanyang Technological University, Singapore
[4]London School of Hygiene and Tropical Medicine, University of London, United Kingdom
[5]Department of Surgery, Li Ka Shing Faculty of Medicine, The University of Hong Kong, China
[6]School of Medicine, University of St Andrews, United Kingdom
[7]Department of Applied Bioinformatics, University of Göttingen, Germany
[8]Department of Plant and Environmental Sciences, University of Copenhagen, Denmark
[9]These authors contributed equally.
✉e-mail: yichieh.lim@ntu.edu.sg, cgkoh@ntu.edu.sg, hyli@ntu.edu.sg

**Running title:**
ILF2 blockade drives R-Loop induced breaks in homologous recombination deficient cancers

## ABSTRACT

Oncogenic signaling drives unchecked proliferation by subverting cellular processes, often at the expense of genome integrity. To survive this inherent genotoxic stress, cancer cells have developed a critical reliance on non-oncogenic stress response pathways to safeguard their genome. Capitalizing on this therapeutic vulnerability, we exploited the dependency of cancer cells on stress-mitigating mechanisms during DNA replication to identify a naturally occurring compound — Molephantin. Here, the derivatization of Molephantin produces NYH002 with cancer-specific toxicity at nanomolar potency. As a small-molecule inhibitor (~450 Da), NYH002 selectively binds the ILF2 complex to disrupt the activity of downstream helicases essential for R-loop resolution. Progressive accumulation of unresolved RNA:DNA hybrids increases the frequency of head-on collisions with the replication machinery, resulting in catastrophic genome-wide DNA double-strand breaks. While elevated cyclin E and E2F1 levels predict NYH002 sensitivity, homologous recombination deficient cancer cells exhibit greater vulnerability, as evidenced by the selective lethality observed in both *in vitro* and *in vivo* models. Collectively, the ILF2 plays a central role in coordinating a series of helicases to safeguard R-loop resolution, which NYH002 leverages to restrict tumor malignancy.

## INTRODUCTION

Cancer cells exhibit an unrelenting demand for high transcriptional activity, placing immense stress on the genomic landscape where transcription and replication machineries often converge at the same DNA regions. This simultaneous engagement disrupts the independent coordination required for genome stability, leading to transcription-replication conflicts (TRCs) (1). A consequence of TRCs is the

formation of pathological R-loops, RNA:DNA hybrid structures that, when left unchecked, can obstruct replication fork progression (2). Collisions between these elements can serve as a fundamental driver for induced mutagenesis, particularly in rapidly proliferating cancer cells, where intermittent occurrences of these events act as initiation points for malignant transformation (3). Paradoxically, excessive R-loop formation at high frequency pushes cancer cells toward a precarious state of overwhelming DNA damage, forcing them to rely on an overburdened post-replication repair system such as homologous recombination (HR) for survival (4, 5). The reliance on pathological R-loops to provoke stress-induced mutations that accelerate malignant progression represents an exploitable vulnerability (6).

By deliberately augmenting R-loop formation and impairing their resolution, therapeutic strategies can exacerbate replication-induced DNA breakages via head-on collisions to surpass the threshold necessary for preserving genomic integrity and ultimately triggering a state of replication catastrophe. Persistent genomic stress not only reprograms a pro-tumorigenic mechanism into a lethal weakness, but the resulting unresolved DSBs also provide a rational framework for the selective elimination of cancer cells while sparing normal tissues with inherently lower replication stress.

Here, we uncover an uncharacterized role of interleukin enhancer binding factor 2 (ILF2), which functions in concert with several helicases to suppress pathological R-loop formation. Targeted inhibition of this pathway by the derivatized Molephantin, NYH002, induces selective cytotoxicity in cancer cells exhibiting $G_1$/S-phase dysregulation, especially those with compromised HR repair. Our discovery provides insight into ILF2's complex role in preserving genomic stability while also presenting a therapeutic paradigm that exploits vulnerabilities in cancer-specific stress-mitigation pathways to enhance targeted therapies.

**Naturally Occurring Molephantin Displays High Potency and Cancer Selectivity**

Emerging evidence suggests that cancer-specific toxicity may hold therapeutic potential (7, 8). To investigate this premise, we conducted a retrospective observational study to evaluate patient responses to integrative medicine protocols involving orally administered phytotherapeutic agents (PAs). Our objectives were to characterize clinical outcomes and elucidate the mechanisms of action underlying their therapeutic effects. Of the 27 subjects evaluated for eligibility, 20 were excluded due to ineligibility, withdrawal of consent, or non-compliance with the follow-up protocol (Fig. S1A). Consequently, the cohort comprised of three treatment-naïve patients and four post-first-line treated patients, all of whom had completed a minimum of six-month integrative medicine regimen, with progression-free survival and disease regression evaluated as the primary and secondary endpoint, respectively. Over the 1.5-year follow-up period, routine clinical evaluations documented therapeutic benefits in five patients, with no observed adverse events (Fig. S1B–C and 1A). Notably, three treatment-naïve patients exhibited a marked reduction in antigen levels and tumor size during the six-month treatment, with the remaining patients demonstrating progression-free survival (Fig.1B–C).

Therapeutic activity based on the commonly administered PAs was subsequently evaluated in DLD1 cells where *Elephantopus tomentosus L.,* demonstrated anti-proliferative properties (Fig. 1D–1F). Bioassays indicated growth inhibition, prompting the targeted isolation of bioactive compound(s) from the crude extract. Sequential fractionation by flash column chromatography and monitored by thin-layer chromatography (TLC), revealed distinct compound distributions across the collected fractions. Fractions displaying similar TLC profiles were consolidated and further refined by gel permeation chromatography. Subsequent nuclear magnetic resonance (NMR) spectroscopy confirmed the high purity and structural integrity of Molephantin and Molephantinin (Fig. S1D and 1G). Designated as NYH001 (Molephantin) and NYH101 (Molephantinin), these natural germacranolide sesquiterpenes compounds exhibited effective therapeutic activity within the micromolar range. Among the two, NYH001 demonstrated greater potency as a small-molecule inhibitor (Fig. S1E and 1H). To evaluate the cancer-specific toxicity of NYH001, we treated a panel of 10 solid cancer cell types with the same compound. BJ-5TA, a non-tumorigenic fibroblast cell line was included as a control in the assessment. The latter exhibited the least sensitivity to NYH001 ($EC_{50}$ = 4.67 μM) as compared to the cancer cell panel which responded with an $EC_{50}$ range of 0.82 μM to 4.22 μM (Fig. 1I). Furthermore, NYH001 treatment at 25 mg/kg in HCT116 tumor-bearing animal models demonstrated consistent therapeutic efficacy in mitigating tumor progression while exerting minimal systemic cytotoxicity (Fig. 1J–K).

**NYH002 Suppresses Cancer Growth by Disrupting DNA Integrity**

The isolated NYH001 possesses a rare 10-membered macrocyclic backbone incorporating an (E,Z)-dienone moiety (C1–C4), which is fused with an α-methylene-γ-butyrolactone ring and features four contiguous stereogenic centers (C5-C8) (9). This intricate structure suggests the molecule may exhibit distinctive biological activity, as previously evidenced by its selective induction of cytotoxicity in solid cancer cell lines while sparing non-tumorigenic cells. Hence, we employed a structure-activity relationship approach to exploit the versatile scaffolds of aromatic carboxylate derivatives for the development of lead candidates to systemically explore the molecular mechanism of Molephantin. Five compounds, designated from NYH002–NYH006 were differently synthesized to improve the interactions with nucleophilic residues within the target protein, thereby enhancing therapeutic efficacy (Fig. S2A and 2A). Our strategy enhances the drug-protein binding affinity while simultaneously reducing off-target interactions.

Treatment of a panel of 10 solid cancer cell lines (U251, MB231, A2780, H1299, HUH7, CAPAN1, AGS, A673, DLD1 and PC3) with NYH002–NYH006, revealed these compounds could achieve an $EC_{50}$ at the high nanomolar range (Fig. 2B). All five derivatives exhibited improved efficacy with NYH002 having the highest potency (Fig. 2C). For a therapeutic safety evaluation, animals were daily administered with the top two lead candidates, NYH002 and NYH003 by intraperitoneal route for two weeks. Not only did NYH002 show favorable tolerability *in vivo*, its therapeutic efficacy to elicit cancer cell death also exceeded that of the original NYH001 (Fig. 2D–E).

We next utilized a systems biology approach to determine the signaling network perturbed by NYH002. DLD1 cells received NYH002 treatment followed by tandem mass tag (TMT) labeling in conjunction with liquid chromatography-tandem mass spectrometry (LC-MS/MS) analysis (Fig. S2B). A total of 6,297 labeled proteins were then filtered for differentially expressed proteins (DEPs) which 71 down-regulated proteins were determined. Pathway enrichment analysis of this downregulated protein set indicated NYH002 as a disruptor of post-replication repair (Fig. S2C–D and 2F). To substantiate this finding, transcriptome analysis was also conducted to provide a more comprehensive assessment of the pharmacoproteomics (Fig. S2E). Integration of both omics datasets supported the potential role of NYH002 in perturbing the replication machinery (Fig. S2F and 2G). This prompted the investigation into the integrity of DNA synthesis. Following 24 hours of NYH002 treatment, DLD1 cells exhibited $G_2$/M phase arrest, a critical checkpoint for resolving DNA strand breakages prior to cell division (10). Notably, we observed gross chromosomal breaks in NYH002-treated DLD1 cells from unresolved DNA lesions (Fig. 2H–I). Likewise for the recruitment of γH2AX and 53BP1 to the nucleus as an indicator of DSB regions, these factors are frequently observed near stalled replication forks (11, 12). In NYH002-treated DLD1 cells, the accumulation of γH2AX and 53BP1 foci was indeed associated with intensely stained-DAPI nuclei (Fig. 2J–K) and is not a direct cause of oxidative stress-induced DNA damage (Fig. S2G).

**DNA Strand Breaks Arise from Collisions Between Transcription and Replication Machinery**

Building on our observed evidence of DNA DSBs occurring in a cell cycle-dependent manner, we systematically investigated whether NYH002 induces replication stress. Pulse-chase imaging using our NYH002-alkyne (NYH002P) azide-activated fluorescent (AF594) revealed rapid nuclear localization of the compound with minimal detection in the cytoplasm (Fig. S3A and 3A). Synchronized $G_1$/S-phase DLD1 cells, upon release from aphidicolin (APH) and treatment with NYH002, exhibited high accumulation of γH2AX foci when progressing into S-phase (Fig. S3B–E and 3B). In contrast, CDK1 (RO-3306) synchronized G2/M-phase DLD1 cells which were subjected to the same treatment condition and transitioning into $G_1$-phase showed negligible DNA strand breakages. Furthermore, DNA fiber combing demonstrated a lack of ongoing replication and increased fork stalling (Fig. S3F and 3C). This series of findings provides compelling evidence that NYH002 acts in proximity to the replication machinery to facilitate fork collapse.

We therefore conducted high-throughput chromosome conformation capture (Hi-C) sequencing on NYH002-treated DLD1 cells to examine structural abnormalities in chromatin organization to delineate the mechanisms underlying replication dynamics disruption. In each of the depicted gene sets, alterations in topologically associating domains (TADs) at their transcription start sites (TSSs) remained unchanged, except for the downregulated gene set (Lost <1), which exhibited a gain in chromatin interactions (Fig. 3D). The high-contact-frequency chromatin compaction is restricted to short genomic distances, such as those identified in *NFKB1* locus where there was a shift in loop interaction (Fig. 3E–F). These condensed nuclear regions, marked by H3K27me3 expression (Fig. 3G), could be a direct consequence of RNA polymerase II (RNAPII) stalling caused by TRCs (13). To this end, immunoblotting of NYH002-treated DLD1 cells confirmed the retention of RNAPII, which also coincided with the

induction of DNA DSBs and chromatin condensation, as evidenced by γH2AX activation and increased HP1 expression, respectively (Fig. 3H).

TRCs likely arise from RNA:DNA hybrid formation induced by NYH002 (Fig. S3G–H and 3I) (14). To test this hypothesis, we examined the spatial proximity between the transcription machinery and DSBs by assessing the co-localization of RNAPII and γH2AX foci in NYH002-treated DLD1 cells (Fig. 3J) (14). In line with this, inhibition of transcription elongation using the DRB inhibitor significantly reduced replication-associated DSBs, which is consistent with TRCs driving DNA damage in response to NYH002 treatment (Fig. 3K). The TRC-dependent DSB-induced genome instability raised the question of whether R-loop removal would disrupt NYH002's mechanism of action. To investigate this phenomenon, DLD1 and H1299 cells were transduced with an RNase H1-expressing vector to catalyze the cleavage of ribonucleotides in R-loop substrates, followed by NYH002 treatment. We observed that RNase H1-expressing cancer cells exhibited a marked reduction in γH2AX foci accumulation after NYH002 treatment, which was accompanied by improved overall survival, as revealed by the higher $EC_{50}$ of NYH002 (Fig. S3I and 3L–N).

**NYH002 Targets R-Loop Dynamics by Modulating ILF2-Dependent Helicase Function**

The experimental findings presented thus far establish that NYH002 impairs R-loop resolution to allow the persistence of these pathological RNA-DNA hybrids to interfere with replication fork progression. If this evidence holds true, NYH002 may target a key resolving factor critical to R-loop homeostasis. To identify this putative target, we conducted a competitive binding assay pairing NYH002 (antagonist) with its biotinylated derivative (NYH002P, interactor) (Fig. S4A and 4A). Our approach revealed a single high-affinity interactor at ~48 kDa, implicating a previously uncharacterized protein in R-loop regulatory dynamics (Fig. 4B). This unidentified high-affinity (core) interactor of NYH002P, along with the remaining associated proteins, was subjected to LC-MS/MS analysis to determine the composition of the protein complex. (Fig. S4B). Peptide identification revealed a total of 795 proteins. However, only 183 of these corresponded to the expected molecular weights of the excised silver-stained gel band regions (Fig. S4C and 4C). By leveraging the core and associate interactor sets to sequentially annotate protein-protein interaction (PPI) with respect to CORUM curated nuclear complexes (15), we identified an interaction network that consists mainly of DNA/RNA binding and transcription proteins (Fig. S4D and 4D).

Immunoprecipitation of NYH002P utilizing whole cell lysate (WCL) to investigate all uniquely identified DNA/RNA-binding and transcription-related proteins, including one representative from both the translation cluster and heterogeneous nuclear ribonucleoproteins, uncovered a novel protein complex comprising of eight distinct members (Fig. S4E and 4E–F). Independent assessment based on amino acid sequence homology among the eight candidate proteins confirmed a high confidence interacting complex (Fig. S4F and 4G). Notably, the molecular weights of ILF2, YB1, and HuR were consistent with the approximate ~48 kDa immunoblot band, positioning these three proteins as plausible candidates for the core interactor of NYH002. With the implementation of proximity ligation assay (PLA) to analyze

the quantitative and spatial characteristics of each protein in this uncharacterized complex, ILF2 was identified as the primary interacting partner of NYH002P (Fig. S4G–H and 4H). The cellular thermal shift assay (CESTA), which evaluates protein thermostability in the presence of drug binding, provided further confirmation of the physical interaction between ILF2 and NY002 (Fig. 4I) (16).

Accordingly, we investigated the mechanism by which NYH002 modulates ILF2 function, leading to the destabilization of the protein complex. Immunoblot analysis revealed that the treatment with NYH002 did result in a coordinated downregulation of all members of the complex, a pattern that was recapitulated upon ILF2 knockdown via siRNA (Fig. 4J–K). Notably, ILF2 depletion in DLD1 cells alone was sufficient to recapitulate phenotypic features of NYH002's mechanism, namely the accumulation of unresolved R-loops and the displacement of single-stranded (ss)DNA (Fig. 4L–M). This series of phenotypic observations supports the role of ILF2 as a mediator of replication stress which ultimately led to fork collapse as evidenced by the increased accumulation of γH2AX foci (Fig. 4N).

Although ILF2 has been vaguely implicated in R-loop regulation, the precise mechanism underlying this process remains uncharacterized (17). Our PLA data on NYH002P interaction provided evidence that ILF2 associates with DNA/RNA-binding proteins. This observation suggests a role for ILF2 complex in coordinating with these elements to facilitate R-loop resolution. Immunoblot analysis of NYH002-treated and ILF2-depleted DLD1 cells revealed similar downregulation of DExH-box helicase 9 (DHX9), senataxin (SETX), and Werner syndrome helicase (WRN), helicases which are essential for maintaining R-loop homeostasis (Fig. 4O–P) (18, 19). However, immunoprecipitation of NYH002P showed direct interaction with DHX9 but not with SETX or WRN (Fig. 4Q). PPI based on STRING analysis supported the argument that ILF2 regulates SETX and WRN through DHX9 interaction (Fig. 4R). This prediction was corroborated by our immunoprecipitation and PLA results, which showed a direct interaction between DHX9 and both SETX and WRN (Fig. S4I–K and 4S). In contrast, ILF2 did not exhibit physical binding to either SETX or WRN (Fig. S4L–M). This series of evidence reinforced the notion that NYH002 inhibitory effect of R-loop resolution is mediated through the targeting of ILF2-DHX9 axis (Fig. 4T).

**NYH002 Demonstrates Therapeutic Potential in Both Monotherapy and Combination Treatment**

Elucidating NYH002's mechanism of actions reveals its potential as a concomitant therapy to enhance first-line DNA-damaging treatments by enhancing irreversible DNA strand breakages to trigger apoptosis, despite an intact post-replication DNA repair system (Fig. S5A). To test this rationale, we leverage the enhancement of RNA:DNA hybrid accumulation to exacerbate R-loop burden while simultaneously introducing non-toxic DNA lesions to promote replication stress. NYH002 in combination with clinically approved chemotherapeutic agents – temozolomide (TMZ) and 5-fluorouracil (5FU), with methyl methanesulfonate (MMS) serving as a positive replication stress inducer, demonstrated a synergistic effect (Fig. 5A) (20, 21). At $EC_{50}$ concentration, these clinical chemotherapeutic drugs alone were sufficient to promote replication-dependent DSBs in the form of γH2AX foci but not the induction of DNA damage-mediated apoptosis (Fig. 5B–C). Treatment with NYH002 at approximately $EC_{25}$ concentration also yielded a similar outcome with minimal γH2AX foci formation and the absence of

apoptosis in DLD1 cells. Conversely, the concurrent administration of NYH002 with TMZ, 5-FU, or MMS led to a marked increase in cellular stress, as evidenced by the persistence of unresolved γH2AX foci and cleaved caspase-3. As a proof-of-concept to validate the clinical relevance of this concomitant therapeutic strategy, we investigated the most effective combination, TMZ and NYH002, at 25 mg/kg and 10 mg/kg, respectively, in an animal model. The outcome after alternate day treatment over nine weeks showed complete suppression of tumor progression in concomitantly treated animals (Fig. 5D).

Current evidence supporting this concomitant therapeutic approach reinforces the notion that $G_1$/S checkpoint-deficient tumors, characterized by their intrinsic vulnerability to replication-induced DSBs (22), are likely to exhibit heightened sensitivity to NYH002 monotherapy. The identification of predictive marker/s for $G_1$/S checkpoint deficiency (Fig. S5B–C), demonstrated a strong correlation among *CCNE1*, *E2F1*, *E2F2*, and *CDC25A* genes (Fig. S5D) which included their significance in stratifying patient prognosis (Fig. S5E). Leveraging on the identification of *CCNE1* and *E2F1* as top predictive markers for NYH002 monotherapy in $G_1$/S checkpoint-deficient tumors as supported by their association with *RB1* mutation (Fig. S5F), we curated the CCLE database to identify tumor models exhibiting differential expression of both genes. To establish a pan-cancer model system, we selected two pairs of cell-lines for comparative analysis. The first pair-match, MCF7 and MDA-MB-436 cells, represents breast cancer as a lineage-specific tumor model. The second non-pair match, comprising glioblastoma U251 and osteosarcoma U2OS cells, will serve as a cross-cancer comparator (Fig. S5G). Together, these four cancer cell lines will establish a therapeutic framework for targeting $G_1$/S checkpoint deficiency in a pan-cancer context. Immunoblot analysis confirmed the elevated expression of CCNE1 and E2F1 in MDA-MB-436 and U2OS, which corresponded to a higher baseline of unresolved DNA damage caused by replication stress (Fig. 5E–H). Notably, at increasing concentrations of NYH002, which targeted R-loop resolution, MCF7 and U251 exhibited minimal response. In contrast, MDA-MB-436 and U2OS showed sensitivity to NYH002, as evidenced by the presence of S9.6 expression and progressive increase in γH2AX foci numbers (Fig. S5H and 5I–J). Furthermore, in cell survival analysis, $G_1$/S checkpoint-deficient MDA-MB-436 and U2OS cells displayed marked susceptibility to NYH002, whereas $G_1$/S checkpoint proficient MCF7 and U251 cells exhibited greater tolerance, revealing the vulnerability of $G_1$/S deficient cells to NYH002 therapy (Fig. 5K–L).

**NYH002 Exploits DNA Repair Vulnerabilities to Unmask Therapeutic Potential in HRD Cancers**

The increased sensitivity of $G_1$/S checkpoint-deficient tumors to NYH002 treatment is likely a direct consequence of a compromised DDR cascade (23). With the excessive accumulation of unresolved R-loops during the S-phase cell-cycle because of ILF2-DHX9 axis inhibition, this critical failure can overwhelm the cancer cells' repair capacity to resolve replication-dependent DSBs. By analyzing a curated cohort of 9,880 solid tumors in a pan-cancer setting, we established a positive correlation between high CCNE1 and E2F1 expression and the presence of 70 and 34 mutated DDR genes, respectively (Fig. S6A–B). In agreement with this observation, differential expression of CCND1 and CDK4, which governed the $G_1$-phase cell-cycle progression did not correlate with changes in DDR

mutations (Fig. S6C–D). Venn diagram analysis illustrated that 31 genes were shared between high-expression CCNE1 and E2F1 (Fig. S6E–I). Using this common DDR gene set, pathway enrichment concluded that most $G_1$/S checkpoint-deficient tumors had a limited HR repair capacity (Fig. S6J–K). Hence, we investigated the context of pathway lethality by performing a loss-of-function analysis using a siRNA library that targets the DDR cascade (n=239). This independent yet unbiased approach enabled a systematic evaluation of the functional contributions of key genes within the DDR network. Our findings identified 209 knockdown genes that conferred selective vulnerability to NYH002-treated DLD1 cells, with the majority implicated in the response to DSBs (Fig. 6A–B). Pathway enrichment using the top 90th percentile of DDR genes revealed a critical role of HR in survival dependency (Fig. 6C). Recognizing the pivotal role of a limited post-replicative repair mechanism in mediating susceptibility to NYH002 treatment, we investigated the top three candidate HR genes, exonuclease 1 (EXO1), mutS homolog 3 (MSH3) and flap structure-specific endonuclease (FEN1) that were identified by the siRNA DDR library for synthetic lethal interaction (Fig. S6L and 6D) (24-26). Here, we moved beyond the reliance on breast cancer (BRCA) 1/2 mutations and utilized genomic scar assessment (Fig. S6M) to capture a broader spectrum of HR deficiencies (27). Using a cut-off score of ≤42, we interrogated the CCLE database to identify representative cancer cell lines from each major solid tumor type exhibiting HR proficiency (28, 29). An HR-deficient (HRD) cell line (score >42) was included as a positive control (Fig. S6N). Notably, siRNA-mediated depletion of EXO1, MSH3, or FEN1 exacerbated NYH002 sensitivity (approximately $EC_{25}$) in all HR-proficient cancer cell lines, resulting in near-complete ablation of cell growth (Fig. 6E). This effect was, however, absent in the HR-deficient CAPAN-1 cell line, which had already exhibited pre-existing susceptibility to NYH002. Further depletion of EXO1, MSH3, or FEN1 did not exacerbate growth inhibition in NYH002-treated CAPAN-1 cells.

In our preclinical assessment, we identified and selected the most frequent occurring HRD tumor type in the CCLE dataset as a representative model to investigate the therapeutic potential of NYH002 in selectively targeting defective HR malignancies (Fig. S6O–P). Based on this analysis, we prioritized our focus on lung and breast cancers. Clonogenic and cell viability assays confirmed that H1299 (lung) and MDA-MB-436 (breast) cells with HRD exhibited significant vulnerability to NYH002 therapy, whereas their HR-proficient counterparts, A549 and MDA-MB-231, exhibited greater tolerance under the same treatment conditions (Fig. S6Q and 6F). Our dose escalation assay in healthy non-tumorigenic animals determined that 25 mg/kg of NYH002 represents the relative minimum effective dose with complete drug clearance observed by 24h (Fig. S6R and 6G). Intraperitoneal administration of NYH002 at this concentration led to widespread distribution across all major organs within 6 hours, as confirmed by LC-MS/MS. Given the molecular weight of NYH002 is approximately 450 Da, the ability of this small molecule to penetrate the blood-brain barrier is consistent with its physicochemical properties (Fig. 6H) (30). Importantly, there was no adverse and chronic systemic cytotoxicity even after two weeks of intraperitoneal administration and this finding was corroborated by stable blood counts (Fig. 6I) and an absence of cell death, as confirmed by H&E staining of the liver and kidney (Fig. 6J–K). Across the four xenograft models encompassing both HRD and HRP subtypes of lung and breast cancer, administration of NYH002 at a dosage of 25 mg/kg consistently reduced tumor growth rate in all animals (Fig. 6L–O).

Its therapeutic efficacy, however, was remarkable in HRD tumors, where growth was abrogated, highlighting NYH002's selective cytotoxicity against malignancies with compromised HR (Fig. S6S–T).

## DISCUSSION

The presence of R-loop represents a fundamental paradox, indispensable for cellular functions yet detrimental when their aberrant accumulations interfere with DNA duplication, leading to replication stress, DNA breakage, unstainable repair and ultimately cellular death (31). Here, our findings reposition ILF2 in a previous unrecognized role in regulating R-loop homeostasis to shield the genome against the cascading consequences of replication-induced DNA breakages. The mechanism underlying ILF2's role hinges on its interaction with DHX9 at transcription sites (32, 33). In this position, DHX9 facilitates the unwinding of stable RNA:DNA hybrids to prevent impending conflicts with the replication machinery while assisting RNAPII in the binding of DNA to initiate nascent RNA production (33, 34). These findings are consistent with our observation of reduced TSSs and the accumulation of RNAPII in the event of unresolved R-loops (35). Similar to DHX9, several helicases including SETX and WRN also play independent roles in unwinding RNA:DNA hybrid structures (18, 36). BRCA1 and DDX17 are known recruiters for SETX, analogous to CK2 in activating WRN to initiate R-loop resolution (19, 37). The presence of parallel pathways highlights the necessity of redundancy to ensure the timely removal of pathological R-loops and prevent the interference with the replication machinery. Our work offers an alternate perspective in which ILF2 overrides these independent pathways. Depletion of ILF2 decisively triggers a cascade of downregulated proteins through the DHX9 axis, including SETX and WRN, while also impacting other helicases such as DDX3X, DDX5, and DHX15 (38-40). Given its potential role as an upstream regulator in R-loop resolution, the presence and frequent overexpression of ILF2 in solid cancers, as revealed by the Human Protein Atlas, is unsurprising (41). Its universal expression, combined with a near absence of identifiable mutations, supports the notion that ILF2 functions as a non-oncogene, serving as a survival mechanism to mitigate genetic stress induced by oncogenic signaling (42).

It is precisely this series of uncharacterized mechanisms of action that led to the discovery of Molephantin as a first-in-class ILF2 inhibitor. NYH002-treated cancer cells phenocopy ILF2 depletion in causing pathological R-loops, while non-tumorigenic cells showed greater tolerance. Our PK/PD assessment further demonstrated that the serum concentration required for NYH002 to effectively impede tumor progression is readily achievable without inflicting chronic adverse side effects. Additionally, an independent phenotypic study corroborated our findings, confirming that Molephantin exerts selective cytotoxicity against high-grade cancers (43). These results align with the retrospective observational data, where cancer patients undergoing integrative medicine exhibited absence of long-term or severe side effects. Importantly, routine medical assessments and patient-reported outcomes indicated either stable disease or tumor reduction.

The stark contrast in treatment sensitivity between healthy normal and tumorigenic cells can be explained by our model (Fig. 7). Tumors with $G_1$/S deficiency have considerable replication stress.

When NYH002 disrupts this process by introducing unresolved R-loops, these tumors encounter a higher frequency of TRCs, leading to replication-induced DNA breakages. In response, these tumors rely on post-replicative HR as a primary source of repair. We exploited this dependency by combining NYH002 with different alkylating agents, driving DNA DSB accumulation beyond the threshold of repairability. To further examine this therapeutic strategy, we extended the investigation to uncover vulnerabilities in HR-deficient cancer cells that are independent of BRCA1/2 status to broaden the treatment potential of NYH002 (29). Here, our data provide several lines of evidence supporting the concept that synthetic lethality between ILF2 inhibition and HR deficiency arises from disrupting R-loop homeostasis. We show that NYH002 interacts in close proximity to R-loops to impair their resolution and consequently drive TRCs. Furthermore, overexpression of RNase-H1 mitigates NYH002-induced R-loop accumulation, thereby reducing replication-induced DNA breakages. The identification of synthetic lethal gene pairs, such as EXO1, in NYH002-treated cells supports this mechanistic link, along with the treatment susceptibility observed across multiple solid cancer types depleted of EXO1. Lastly, NYH002 therapy suppresses tumor progression in both BRCA-deficient xenograft and orthotopic models. Our study presents a mechanistic insight that aligns with recent reports demonstrating two different strategic synthetic lethality approaches: disrupting transcription factors to increase R-loop accumulation in HR-deficient cells, and, enhancing the displacement of exoribonucleases in cancer cells that are burdened by excessive R-loop formation (14, 44). Together, these findings establish a mechanistic link between ILF2 inhibition by NYH002, HR deficiencies, and R-loop dysregulation, thereby providing a therapeutic framework for exploiting this vulnerability specifically in stress-mitigating cancer cells.

## MATERIAL AND METHODS

### Human and Animal Ethics

Patient recruitments were carried out in accordance with the approval of the Institutional Review Board of Nanyang Technological University (NTU), Singapore (IRB-2022-768). For animal studies, experiments were conducted in accordance with the recommendations of the National Advisory Committee for Laboratory Animal Research guidelines, under the Animal & Birds (Care and Use of Animals for Scientific Purposes) Rules of Singapore. The Institutional Animal Care and Use Committee of NTU approved the current protocol (No. 22049).

### Observational Study

In a retrospective research initiative conducted offsite at NTU, patients who had previously undergone integrative medicine treatment were invited to participate in an observational study. Participant eligibility was assessed in accordance with the approved protocol (IRB-2022-768). Evaluation was based on a review of participants' past medical histories, with a specific inclusion criterion stipulating a minimum six months of integrative medicine use. The integrative medicine regimen comprised an oral administration of combined phytotherapeutic agents (PA) which were derived from medicinal plant materials. Additional criteria included the conduct of questionnaires, and the collection of routine pathological reports of biomarkers and/or medical imaging conducted before and after the integrative

medicine treatment. Informed consent was obtained from all patients, and their biographical data were de-identified to maintain confidentiality. Financial compensation was not offered for participation in this study.

**Cell Culture**

Unless otherwise stated, all cell lines were grown in culture medium supplemented with 10% fetal bovine serum (FBS) (Thermo Fisher Scientific) and 1% penicillin/streptomycin (Cytiva). DLD-1, HCT116, H1299, Huh7, AGS, PC3, A2780, and A673, A549, HepG2, LnCAP cells were cultured in RPMI1640 Medium (Gibco). MDA-MB-231, MDA-MB-436, U2OS, and U251 were cultured in DMEM (Gibco). Capan-1 was cultured in IMDM (Gibco) supplemented with 20% FBS and 1% penicillin/streptomycin. BJ-5Ta was cultured in a 1:1 ratio of DMEM and Medium 199, supplemented with 10% FBS, 1% penicillin/streptomycin, and 0.01 mg/ml hygromycin B (Nacalai Tesque). All cells were cultured in a humidified incubator at 37°C with 5% $CO_2$, routinely screened for mycoplasma contamination, and authenticated by STR profile to verify their authenticity.

**Phytotherapeutics**

Medicinal plant materials, PA1 (*Clinacanthus nutans*), PA2 (*Strobilanthes crispa L*), PA3 (*Elephantopus tomentosus L*), PA4 (*Leea indica*), PA5 (*Houttuynia cordata*), and PA6 (*Zebrina pendula Schnizl*) were cleaned, cryodesiccated and grounded into a fine powder with a laboratory-grade BioloMix grinder. To achieve bioactive extracts, the powdered materials were suspended in 60% aqueous ethanol at a ratio of 1:30 (w/v) and subjected to continuous agitation at room temperature. Mixture was centrifuged, and the resulting supernatant was concentrated overnight at 37°C using a vacuum centrifuge (Concentrator Plus, Eppendorf, USA). The dry pellet was weighed and stored at 4°C. As a ready-to-use bioactive extract, the pellet was resuspended in sterile water.

**Chemicals**

APH, RO-3306, MMS and 5FU were purchased from Sigma-Aldrich. TMZ and DRB were obtained from MedChem Express and Merck, respectively.

**RNA Interference**

The human ON-TARGET*plus* DDR siRNA library (Dharmacon) was obtained as SMARTpool reagents, each comprising a mixture of four siRNAs targeting a single gene. A list of 239 genes is available in the supplementary. Additional ON-TARGET*plus* siRNA was also purchased for *EXO1*, *MSH3*, *FEN1* genes. siRNA negative control was obtained from Dharmacon.

**Plasmid**

pEGFP-RnaseH1 plasmid was a kind gift from Dr. Kah Suan Lim, National Cancer Centre Singapore.

**Public Datasets**

Genomic, exon and RNA-seq datasets were obtained from TCGA (45).

**Bioactive Compounds**

PA3 crude powder (40 g) was sonicated in ethyl acetate and decanted repeatedly to achieve a greenish-yellow supernatant. The combined crude extracts were then filtered over Celite®, concentrated *in vacuo*, and purified by flash column chromatography (FCC) on silica gel (n-hexane/ethyl acetate, 4:1 to 1:1). Purified material in ethyl acetate was treated with charcoal for 30 minutes before passing through Celite®. The filtrate was concentrated under reduced pressure and further purified by gel permeation chromatography (LaboACE LC-5060, JAIGEL-2HR-40 column; 24 mg/ml; 10 ml injection; 30 ml/min flow rate), affording three fractions: pure Molephantinin (NYH101) and Molephantin (NYH001), and a mixture of both compounds.

**Molephantin Derivatives and Probe**

NYH001 derivatives were synthesized for structure-activity relationships (SAR). Substituted benzoyl chlorides with various functional groups were added to a mixture of NYH001, $Et_3N$, and DMAP in anhydrous $CH_2Cl_2$ at 0°C under argon. The reaction was performed at room temperature and concentrated *in vacuo*. The crude residue was further rinsed with saturated $NaHCO_3$, extracted with dichloromethane, and the combined organic layers were filtered, purified, and further concentrated using FCC on silica gel to produce solids of various derivatives. The structures and qualities of all compounds were examined using $^1$H NMR, $^{13}$C NMR, and MS (ESI). Refer to Extended Material and Methods 1 for detailed protocol and chemical characterization reports.

**Cell Divisions**

Briefly, $2 \times 10^6$ viable single cells were pre-labeled with 10 μM CFSE (Thermo Fisher Scientific). Labeling was quenched with RPMI medium containing 10% FBS. A portion of these cells was fixed and stored at 4°C, while the remaining cells ($5 \times 10^5$) were seeded in fresh medium in a T-25 flask with the appropriate treatment. After four days of culture, cells were harvested and rinsed twice with PBS prior to flow cytometric analysis. Cell proliferation data were analyzed using FlowJo software.

**Cell Proliferation and Therapeutic Synergy**

Cell viability was assessed using MTT [3-(4,5-dimethylthiazol-2-yl)-2,5-diphenyltetrazolium bromide]. Briefly, cells were seeded in 96-well plates at a density of $8 \times 10^3$ to $1.2 \times 10^4$ cells per well the day prior to experimentation. Following the indicated treatment, MTT was added to cells and incubated in the dark at 37°C. Formazan crystals were solubilized with DMSO. Absorbance was measured at 570 nm. Cell viability was calculated as a percentage relative to the untreated control. Half maximal effective concentration ($EC_{50}$) values were calculated using GraphPad Prism. Alternatively, cell viability data were organized into a matrix format for analysis using SynergyFinder 3.0 (46). The Highest Single Agent (HSA) model was selected for its conservative nature, minimizing false positives and reducing the risk of overestimating synergy between two drugs. For selective lethality, the coefficient of drug interaction (CDI) was calculated by dividing the observed cell viability of the combined treatment by the product of the cell viabilities for each individual treatment at the same concentration (47).

**Colony Formation**

Approximately $1 \times 10^3$ cells were seeded into 6-well plates and allowed to attach for 48 hours. The cells were treated with 0.1 μM and 1 μM NYH002 for 1 hour at 37ºC and incubated in fresh media for seven days to allow colony formation. The colonies were fixed in 4% paraformaldehyde and stained with 0.5% crystal violet. Colonies were rinsed with water and air-dried, Images were taken with ChemiDoc MP Imaging System (Bio-Rad). The number and area of colonies were quantified using FIJI software.

**Cell Cycle Profile**

Approximately $6 \times 10^5$ cells were seeded into 6-well plates and treated with NYH002 for 24 hours. Cells were harvested, fixed in -20°C 70% ethanol and stained with propidium iodide staining buffer (0.1% Triton-X, 40 mg/ml propidium iodide, 200 mg/ml RNase A). Samples were quantified with BD LSRFortessa™ (BD Biosciences) and analyzed in FlowJo™ software (BD Biosciences).

**Immunofluorescence Stain**

Cells were seeded onto coverslips in a 24-well plate and allowed to adhere overnight. Following treatment the next day, cells were fixed with 4% paraformaldehyde and permeabilized with 0.2% Triton X-100/ PBS. For S9.6 staining, cells were fixed with ice-cold methanol. All primary antibodies were applied at room temperature, rinsed with TBS/0.1% Tween, and replaced with Alexa Fluor-conjugated secondary antibodies. Nuclei were counterstained with DAPI (1 μg/ml), and coverslips were mounted in ProLong™ Gold Antifade Mountant (Thermo Fisher Scientific). The slides were imaged using a Zeiss Axio Observer.Z1 fluorescence microscope or Zeiss LSM980 confocal microscope. Foci counts were measured with CellProfiler software. Images were converted to grayscale, and a threshold was applied to define foci. Foci were counted per nucleus, with at least 100 nuclei per condition analyzed. Manual verification was performed to exclude artifacts.

**ssDNA Stain**

Naïve ssDNA labeling was performed as previously described (48). Briefly, cells were pulse-labeled with 10 μM IdU for 24 hours prior to treatment, washed with PBS, and pre-extracted with ice-cold CSK buffer (10 mM PIPES, 300 mM sucrose, 100 mM NaCl, 3 mM $MgCl_2$, 0.2% Triton X-100) at room temperature. Cells were then fixed in 2% formaldehyde, blocked in 10% BSA in PBS/0.05% Tween and immunostained with anti-IdU primary antibody and Alexa Fluor 594–conjugated secondary antibody.

**DNA Pulse-Labeled Fiber**

DNA fiber assay was performed as previously described (49). Briefly, cells were pulse-labeled with 20 μM CIdu (Sigma-Aldrich) for 30 minutes at 37°C, treated with NYH002 for 1 hour before labeling with 100 μM IdU (Sigma-Aldrich) for 30 minutes. Cells were then lysed with spreading buffer (0.5% SDS, 200 mM Tris-HCl, 50 mM EDTA) and DNA fibers were stretched on the glass slide. Incorporated analogs were stained using rat anti-BrdU antibody (Abcam) and mouse anti-BrdU antibody (BD Biosciences). Images were acquired with a Zeiss Axio Observer.Z1 fluorescence microscope and at least 200 fibers were quantified for each experiment.

**Chromosome Spread**

Treated cells were harvested and treated in hypotonic buffer (75 mM KCl) at 37°C. The buffer was removed by centrifugation and cells were fixed dropwise with ice-cold methanol/acetic acid (3:1). The cells were spun down at 200× g with the fixation step repeated twice before storing samples at 4°C overnight. The cells were dropped onto glass slides and stained with DAPI (1 μg/ml). Images of the chromosome spread were acquired with Zeiss Axio ObserverZ1 fluorescence microscope.

**Cell Transfection**

pEGFP-RnaseH1 plasmid was transfected into cells using Lipofectamine 3000 transfection reagent (Thermo Fisher Scientific) according to the manufacturer's instructions. All siRNAs were transfected into cells using DharmaFECT1 Transfection Reagent (Dharmacon) according to the manufacturer's instructions.

**Proximity Ligation Assay**

After the indicated treatments, cells cultured on coverslips were fixed with 4% formaldehyde and permeabilized with 0.2% Triton X-100/PBS. PLA was performed using Naveni™ TriFlex Cell MR (Navinvi Diagnostics) according to the manufacturer's instructions. Briefly, cells were immersed in blocking buffer at 37 °C, then incubated overnight at 4 °C with primary antibodies (1:500) diluted in the supplied buffer. Cells were rinsed and incubated with secondary antibodies conjugated with either plus or minus PLA probes. This is followed by ligation and amplification steps. Cells were stained with DAPI before mounting on glass slides. PLA signal was detected using the Zeiss LSM980 confocal microscope under 40× objective lens. The images were analyzed and processed using Zen Blue software. The PLA signal and foci were quantified using the segmentation tool. Automated segmentation parameters were optimized to detect individual PLA foci. The total number of foci per nucleus was calculated, and at least 100 nuclei per condition were analyzed.

**Cellular Thermal Shift Assay**

CETSA was performed following the published protocol (16). Briefly, $1 \times 10^7$ DLD-1 cells were resuspended in PBS supplemented with Halt™ Protease and Phosphatase Inhibitor Cocktail (Thermo Fisher Scientific). Cells were subjected to three freeze-thaw cycles, and lysate was centrifuged at 12,000× g. The supernatant was collected, aliquoted, and incubated with either DMSO or 100 μM NYH002 at room temperature on a rotator for 1 hour. Samples were subjected to a temperature gradient (40–60°C) for 3 minutes using a gradient thermal cycler (Eppendorf) and subsequently incubated at 25°C for 3 minutes before placing on ice. Lysates were centrifuged at 16,000× g, and the supernatant was collected. Prior to SDS-PAGE, Laemmli buffer was added, and samples were denatured at 95°C for 10 minutes.

**Cell Lysis and Immunoprecipitation**

Cell pellets were lysed in ice-cold RIPA or co-immunoprecipitation lysis buffer and centrifuged at 14,000× g to collect supernatants for immunoblotting and immunoprecipitation, respectively. For the

latter, whole-cell lysates (WCL) were pre-cleared with Dynabeads™ M-280 streptavidin or protein A (Invitrogen) prior to protein estimation with Pierce BCA Kit (Thermo Fisher Scientific). Briefly, 10 μM of NYH002P was incubated with 1.5 mg of WCL overnight at 4°C, followed by click chemistry-mediated biotinylation and subsequent incubation with Dynabeads™ streptavidin. Alternatively, 1 μM of antibody was incubated with 1 mg of WCL overnight at 4°C and incubated with Dynabeads™ protein A. Samples were magnetically bounded and washed with lysis buffer and a high-salt (0.5 M NaCl) solution. Bound proteins were eluted with 2× Laemmli buffer (Bio-Rad) at 95°C for 10 minutes.

**SDS-PAGE, Silver Stain and Immunoblot**

Denatured proteins were loaded onto an SDS-PAGE gel and electrophoresed at 120 V for 2 hours. Silver staining of the SDS-PAGE gel was performed according to the manufacturer's protocol (Pierce™ Silver Stain Kit). Alternatively, proteins were then transferred onto methanol-activated PVDF membranes using Trans-Blot® Turbo™ System (Bio-Rad) at 1.3 A for 12 minutes. Membranes were blocked with 5% skimmed milk in 0.1% TBS/T prior to incubation with primary antibodies overnight at 4 °C. The following day, membranes were rinsed with 0.1% TBS/T, followed by incubation with horseradish peroxidase (HRP)-conjugated secondary antibodies. Signal detection was performed using enhanced chemiluminescence (ECL) reagents and visualized with the ChemiDoc MP Imaging System (Bio-Rad).

**Nascent mRNA**

Following the manufacturer's instructions, the nascent mRNA was stained using the Click-iT™ RNA Alexa Fluor™ 594 Imaging Kit (Thermo Fisher Scientific). Cells were seeded overnight at a density of $1.4 \times 10^5$ per 12 mm glass coverslip. The following day, cells were treated with 1 μM NYH002P and incubated with 1 mM 5-ethynyl uridine (EU) in culture media for 1 hour to label nascent mRNA. EU-labeled cells were then fixed with 4% paraformaldehyde and permeabilized with 0.2% Triton X-100. Each coverslip was stained with Click-iT buffer following the recommended manual recipe. The staining buffer was rinsed off, cells were stained with 1 μg/ml DAPI and mounted with ProLong Diamond Antifade Mountant (Thermo Fisher Scientific).

**NYH002P-ClickiT**

NYH002P was labeled and stained using the Click-iT™ EdU Cell Proliferation Kit for Imaging, Alexa Fluor™ 488 dye (Thermo Fisher Scientific) following manufacturer's instructions. DLD-1 were seeded at $1.4 \times 10^5$ cells per 12 mm coverslips and treated with 1 μM NYH002P for 6 hours. Cells were fixed with 4% PFA and permeabilized with 0.2% Triton-X. Each coverslip was stained with freshly prepared buffer as instructed by the kit. The stained coverslips were compatible for further staining with primary antibodies, DAPI, or for PLA experiments.

**RT-qPCR**

Total RNA was extracted using FastPure Cell/Tissue Total RNA Isolation Kit V2 (Cat# RC112-01, Vazyme). Total RNA was reverse transcribed to cDNA using HiScript III All-in-one RT SuperMix Perfect

for qPCR (Vazyme) on a gradient thermal cycler (Eppendorf). qPCR was performed with 500 nM forward and reverse primers (IDT) and Taq Pro Universal SYBR qPCR Master Mix (Vazyme) using Bio-Rad CFX96 Touch Real-Time PCR Detection System with CFX Manager software (Bio-Rad). GAPDH was used as an internal control for normalization, and the relative expression level was calculated by the 2(-Delta Delta C(T)) method. Primer sequences are listed in the supplementary information.

**RNA Sequencing**

The mRNA of treated samples was purified using poly-T oligo-attached magnetic beads and fragmented for cDNA synthesis. Directional and non-directional libraries were prepared with end repair, A-tailing, adapter ligation, size selection, amplification, and purification. Libraries were quantified and sequenced on an Illumina platform. Quality control included adapter trimming, removal of low-quality reads, and calculation of Q20, Q30, and GC content. Reads were mapped to the reference genome using Hisat2, and novel transcripts were assembled with StringTie. Gene expression levels were quantified using FeatureCounts and FPKM. Differential expression analysis was conducted with DESeq2 (biological replicates) using the Benjamini-Hochberg method for multiple testing correction. Genes with an adjusted p-value ≤ 0.05 and absolute fold-change ≥ 2 were considered significantly differentially expressed.

**Proteomics Sample Preparation and Analysis**

For each condition, 100 μg of lysate was loaded for in-solution or in-gel digestion. Samples were reduced, alkylated, and incubated overnight with Pierce trypsin protease, mass spectrometry (MS) grade (Thermo Fisher Scientific). Label-free or TMT10-plex isobaric-tagged (Thermo Fisher Scientific) samples were first loaded onto an Xbridge™ C18 column where peptides were separated based on their hydrophobicity. The separated peptides were delivered through the Dionex EASY-Spray nano-electrospray to be ionized. These ions were introduced into a high-resolution Q Exactive orbitrap. A full MS scan (350–1,600 m/z range) was acquired at a resolution of 70,000 and a maximum ion accumulation time of 100 ms. Raw data files were processed and searched using Proteome Discoverer 2.1 (Thermo Fisher Scientific). SEQUEST algorithm was then used for data searching to identify proteins. The normalization mode was based on the total peptide amount and a false discovery rate (FDR) for protein identification was < 1%. The protein list was further filtered with a minimum of 1 unique and 1 common peptide including matched molecular weight prior to pathway enrichment using KEGG, GO, Reactome and WikiPathway by Cytoscape (50). Alternatively, curated proteins were also performed using STRING and IntAct for PPI or the use of CORUM database to match protein complex (15).

**Orthotopic and Xenograft Models**

Briefly, tumor cells ($1 \times 10^6$) in HBSS were injected subcutaneously into the flank or orthotopically into the mammary fat pad of nude mice. Tumors were allowed to grow till they reached a palpable size of approximately 100 $mm^3$ before randomizing into control and treated groups. NYH001, NYH002 and NYH003 were dissolved in a vehicle solution consisting of 10% Kolliphor® EL, 10% DMSO, and 80%

saline, therapeutics were administered via either the intraperitoneal or intratumoral route. Mice received treatment every other day for two weeks, unless stated otherwise. Temozolomide was dissolved in saline to a concentration of 10 mg/kg and administered orally once daily. Mice were weighed twice weekly, and tumor dimensions were regularly measured using calipers. Tumor masses were calculated as follows: Tumor volume ($mm^3$) = (length × $width^2$) / 2. Mice were euthanized in a carbon dioxide chamber when tumor volume reached 1,800 $mm^3$, weight loss exceeded 20%, or the treatment duration reached two weeks, whichever occurred first.

**Cytotoxicity, Pharmacokinetics, and Biodistribution**

For cytotoxicity assessment, J:NU/Inv mice received intraperitoneal injection of vehicle or 25 mg/kg NYH002 on alternate days for two weeks. After which, blood was collected by cardiac puncture and diluted in PBS containing 1% FBS and 0.1 mM EDTA at a 1:20 ratio, followed by filtration through a 0.45 µm cell strainer and collected in FACS tubes for flow cytometry assessment by cell size and granularity. For pharmacokinetics and biodistribution, BALB/cJ mice received a single intraperitoneal injection of either vehicle or 25 mg/kg NYH002. Blood was collected via cardiac puncture at indicated time points (0–24 hours) and transferred into vacutainer® EDTA tubes (BD). Organs were also harvested and homogenized in parallel. Both sample types were subsequently centrifuged. Serum from blood or supernatant from homogenized tissue was collected and individually mixed with ice-cold acetonitrile (ACN) at a 1:3 ratio. Samples were precipitated at −20 °C overnight. The following day, samples were centrifuged at 4°C, and the supernatant was collected and concentrated. Resulting pellet was resuspended in 50% (w/v) ACN and analyzed by MS.

**Histopathological staining**

Tissues were fixed in 4% PFA, processed and embedded in paraffin, and subsequently sectioned at 5 µm thickness using a rotary microtome. Deparaffinized samples were stained with Mayer's hematoxylin and Eosin Y, then dehydrated with ethanol. The slides were mounted with DPX Mountant for histology (Sigma) and imaged using Axio ObserverZ1 fluorescence microscope (Zeiss) under 20× objective lens.

**Hi-C sequencing**

Hi-C was performed using the Dovetail TopoLink V2 kit, following the default settings and conditions. Libraries were sent to NovogeneAIT for sequencing on Illumina NovaSeq at 300M PE150 reads per sample, with 2 biological replicates per condition. Fastq files from Illumina sequencing were first trimmed with trimmomatic [settings: ILLUMINACLIP: Adapters:2:30:10:8:true \ HEADCROP:5 \ SLIDINGWINDOW:4:10 \ LEADING:3 \ TRAILING:3 \ MINLEN:30]. Reads were aligned on the hg19 genome using bwa default settings. Pairtools was used to prepare the paired interaction using the parse [settings: --min-mapq 10 --walks-policy 5unique –max-inter-align-gap 30], sort [settings: default], dedup [settings: --mark-dups] and split [settings: default] followed by samtools indexing and sorting of resulting .bam files and pairix indexing of resulting .pairs files. Finally, contact matrices were generated using cooler followed by cload [settings: pairix] and zoomify [settings: --balance] commands (51). Pile-ups were generated from .cool contact matrices using coolpup.py and its associated plotpup.py

packages (52). The merge matrices from both replicates of each condition were used for this analysis, as it is not influenced by coverage biases. Hi-C heatmaps were generated from the .cool matrices using HiCExplorer (53). The 2 replicates with the closest coverage quality (U2 and H2 from the shared matrices), at 32 kb resolution, were used for imaging to alleviate coverage biases.

**Illustration**

Proposed model for NYH002 was created with BioRender.com under publication license (MK289PVV3V).

**Data Analysis**

All data presented were obtained from three independent experiments, unless otherwise specified. Significance was assessed using an unpaired, two-tailed Student's t-test, assuming equal variance between the control and experimental groups, when the sample size was 10 or fewer. In the event of a larger sample size (>10), a normality distribution test was conducted using the Shapiro-Wilk Test and QQ-plot. For normally distributed data, a parametric test was used (unpaired two-tailed Student's t-test or two-way ANOVA test). If the data is not normally distributed, the Mann-Whitney U test was employed. The significance of survival probability was calculated using the log-rank (Mantel-Cox) test. A p-value equal to or less than 0.05 was considered statistically significant in supporting the alternative hypothesis, unless stated otherwise.

## RESOURCE AVAILABILITY

**Lead Contact**

Further information and requests for resources should be directed to and will be fulfilled by the lead contact, Dr Lim Yi Chieh (yichieh.lim@ntu.edu.sg), Associate Professor Li Hoi Yeung (hyli@ntu.edu.sg), and Associate Professor Koh Cheng Gee (cgkoh@ntu.edu.sg).

**Materials Availability**

All resources are available upon request to the lead contact.

**Acknowledgements**

We would like to thank A/Prof. Mu Yuguang and Asst Prof. Wilson Goh for their assistance in molecular docking and MS, respectively; Chermaine Choo for facilitating patient interviews; Dr Ming Shan for data collection; Core facilities of SBS, NTU. This study was supported by the Ministry of Education, Singapore (AcRF Tier 1 RG33/23 to H.Y.L), Nanyang Biologics Pte Ltd (REQ0196946 to H.Y.L and C.G.K) and National Research Foundation, Singapore (MOH-001387 and AISG3-GV-2023-014 to M.J.F)

**Declaration of Interests**

H.Y.L. and C.G.K. are shareholders of Nanyang Herbs Pte Ltd. H.Y.L is a shareholder of NYB.AI Pte Ltd. All remaining authors declare no competing interests.

**Author Contributions**

Conceptualization, Y.C.L., S.K.L., C.G.K., and H.Y.L.; Formal analysis, Y.C.L., S.K.L., R.H.Y., Y.K.C., B.L., and H.Y.L.; Investigation and data analysis, Y.C.L., S.K.L., R.H.Y., V.M., C.X.C.S., Y.K.C., B.L., M.W., X.M.D., S.K.T., S.L.Y., R.P., S.Z., J.Y.X.W., and Z.A; Resources, P.S., C.N., M.M., S.C., and M.J.F., and L.L.D.Z.; Supervision, Y.C.L., S.K.L., H.Y.L., and C.G.K.; Visualization, Y.C.L., S.K.L., and R.H.Y.; Writing – original draft, Y.C.L., S.K.L., R.H.Y., and H.Y.L.; Review & editing, all authors; Funding acquisition, M.J.F., H.Y.L., and C.G.K.

**FIGURE LEGENDS**

**Figure 1:** Identification of Molephantin revealed selective cytotoxicity in solid cancers.

A) Sankey plot of recruited cancer patients (n=7) in a retrospective observational study on integrative medicine.

B) Time progression of the prostate antigen level (PSA) in naïve stage IV metastatic prostate cancer patients receiving integrative medicine.

C) CT scan of a naïve prostate cancer patient before and five months after receiving integrative medicine. 'P' denotes the region of the prostate, and 'T' indicates the region of the tumor.

D) Overall view of individual patients receiving integrative medicine, which comprised oral administration of combined PAs for a minimum period of six months.

E) Cell generation was tracked by measuring the fluorescence intensity of CFSE-labelled DLD1 cells treated with vehicle (DMSO) or 0.5, 5, and 50 μg/ml of various PAs for 96 hours. “Parental” CFSE-labelled cells at day 0 were used as the reference for maximum fluorescence intensity in flow cytometry analysis (n=3).

F) A simplified schematic of extract production was generated using various parts of *Elephantopus tomentosus* L., as indicated (left). Cell proliferation was determined at 48 and 72 hours after DLD1 cells received increasing concentration (0 – 1.70 mg/ml) of extract treatment (n=3).

G) Isolation of Molephantin and Molephantinin compounds from young leaf extracts by preparative HPLC.

H) Chemical structures of Molephantin (NYH001) and Molephantinin (NYH101), and their dose-response effects in DLD1 cells. $EC_{50}$ values were determined 48 hours after treatment (n=3).

I) Cancer-specific cytotoxicity as revealed in a panel of tumorigenic (n=10) and non-tumorigenic (n=1) cell lines treated with a dose range of 0.1–10 μM of NYH001 for 48 hours. Data were presented as the average $EC_{50}$ (n=3).

J, K) Nude mice were engrafted with $1 \times 10^6$ HCT116 cells, followed by intraperitoneal treatment with either vehicle or 25 mg/kg of NYH001. Treatment was performed every other day for two weeks with the animals’ weight measured daily. A control cull was executed upon completion of treatment, and individual tumors were excised for assessment.

Data are presented as mean ± SEM. Unpaired two-tailed t-test (I, J, and K). p values $< 0.05$ were considered significant.

**Figure 2:** Lead-optimized NYH001 suppresses replication machinery and causes chromosomal aberrations.

A) Structural analogue of NYH001 derivatives.

B) Dose-response of NYH001 derivatives (NYH002-NYH006) in a panel of 10 different cancer cell lines as indicated. Mean survival was determined at 48 hours post-treatment (n=3).

C) Therapeutic efficacy of NYH001 derivatives. Fold change in mean $EC_{50}$ was assessed across 10 cell lines and presented as pan-cancer data at 48 hours post-treatment. Each derivative was compared to the corresponding NYH001-treated cell line, where individual dot represents the mean $EC_{50}$ of the respective cancer cell line (n=3).

D) Evaluation of systemic cytotoxicity. A total of 21 healthy nude mice were randomly assigned to vehicle, NYH002 and NYH003 treatment arms. Each animal received a total of 14 daily intraperitoneal injections at 25 mg/kg for 2 weeks. Animal weights were recorded before and after treatment to assess animal health.

E) Drug-induced cell death in DLD1 cells following treatment with increasing concentrations of NYH001 and NYH002 (1–10 μM) for 24 hours. An immunoblot was performed with WCL to determine activation of apoptosis by cleavage of PARP, caspase-3, and caspase-7. β-tubulin was used as a loading control

F) Pathway enrichment analysis of the downregulated proteome was performed on DLD1 cells treated with 2.5 μM NYH002 for 24 hours, followed by TMT-labeling of WCL for MS analysis (n=3). Based on KEGG, Reactome, WikiPathways, and Gene Ontology databases, the differentially downregulated proteins were subjected to pathway enrichment analysis.

G) The protein–protein interaction (PPI) network of NYH002-treated DLD1 cells was established using the STRING and IntAct databases. The network was built on the downregulated proteome as the first interactors (primary clusters), followed by the integration of downregulated transcriptome data to identify the second interactors (secondary clusters).

H) Cell cycle profile based on the propidium iodide staining of DMSO- and 2.5 μM NYH002-treated DLD1 cells after 24 hours (n=3).

I) Chromatid breaks in metaphase spread of DLD1 cells treated with DMSO or 2.5 μM NYH002 for 24 hours (n=3). Scale bar: 5 μm.

J, K) Quantitative image-based cytometry of immunolabeled DLD1 cells receiving either DMSO or 2.5 μM NYH002 for 24 hours. Total number of γH2AX or 53BP1 foci and nuclear DAPI intensity were determined for each of >1,000 individual cells (n=3).

Data are presented as mean ± SEM. Unpaired two-tailed t-test (C, D and H), hypergeometric test with Bonferroni step-down (F) and Mann-Whitney U test without p value correction (J and K). p values < 0.05 were considered significant whereas N.S was regarded as not significant.

**Figure 3:** NYH002 induces replication breakages via the collision of pathological R-loops

A) A simplified schematic strategy to determine NYH002 localization in the cellular compartment (left). NYH002-alkyne (NYH002P) was enabled by click chemistry to function as a fluorescent probe. DLD1 cells were treated with 0.5 μM of this compound and fixed at the indicated time points to determine NYH002P localization within the nuclear compartment.

B) Replication-induced fork breakage was assessed by synchronizing DLD1 cell at $G_1$/S-phase with APH or $G_2$-phase with CDK1 inhibitor for 16 hours. Synchronized cells were released from these chemicals (APH-r and CDK1-r) and immediately received 2.5 μM of NYH002 treatment. DLD1 cells were fixed at one- and six-hours post-treatment and analyzed for DNA DSB by γH2AX foci count.

C) Replication fork stalling was assessed by quantifying the total number of ongoing DNA fiber (left) events and the lack of origin firing (right) in DLD1 cells treated with either DMSO or 2.5 μM NYH002 (n = 3).

D) Pile-up interaction at the transcription start site (TSS) of genes with altered or constant expression following NYH002 treatment (left), alongside a volcano plot showing RNA expression of the genes represented within the pile-up (right). The black dashed square indicates a region of increased interaction at the TSS of downregulated genes following NYH002 treatment.

E) Hi-C heatmap at 32kb resolution centered around the downregulated *NFKB1* gene by NYH002 treatment showing distinct effect of chromatin condensation.

F) Transcript expression of *NFKB1* gene in DLD1 cells was determined by RT-qPCR after 24 hours treatment with DMSO or 1 μM of NYH002 (n=3).

G) Chromatin condensation was determined by H3K27m3 expression in the nucleus of DLD1 cells treated with DMSO or 1 μM of NYH002 for 24 hours (n=3). Arrow in white indicates orientation of direction. Scale bar: 5μm.

H) Immunoblot of transcription stalling in DLD1 cells treated with DMSO or 1 μM NYH002 for 24 hours, as determined by RNAPII (CTD), γH2AX and HP1 expression levels. GAPDH was used as loading control.

I) Presence of R-loops and their proximity to NYH002 localization were assessed 24 hours after treatment with 1 μM of the compound's probe, followed by click chemistry with AF549 fluorophore and immunofluorescence staining using the S9.6 antibody in DLD1 cells. Arrow in white indicates orientation of direction. Scale bar: 5μm.

J) Collision between replication and transcription machinery was determined by the co-localization events of RNAPII (POLR2A) and γH2AX foci post-24 hours after treatment with DMSO or 1 μM NYH002 in DLD1 cells (n=3).

K) Dissolution of TRC through transcription inhibition by DRB (50 μM) was carried out one hour prior to the treatment of 1 μM NYH002 in DLD1 cells. Cells were examined 24 hours later for the presence of DNA DSBs by quantifying total cell number with >5 γH2AX foci (n=3).

L, M) Phenotypic profile of R-loops was assessed in DLD1 cells transfected with empty vector (EV), or RNase H1 for 24 hours, followed by treatment with 1 μM NYH002 for an additional 24 hours. Immunofluorescence staining was then performed using either the S9.6 or γH2AX antibody.

N) Reduction in NYH002 efficacy was assessed in a dose-dependent manner in DLD1 and H1299 cells transfected with either RNase H1 to resolve R-loops or with an empty vector. Cell viability was measured 48 hours post-treatment and data were presented as mean $EC_{50}$ of NYH002 (n=3).

Data are presented as mean ± SEM. Mann-Whitney U test without p value correction (A, J, L and M). Unpaired two-tailed t-test (B, C, K and N). p values < 0.05 were considered significant whereas N.S was regarded as not significant.

**Figure 4:** Targeting the ILF2-DHX9 axis by NYH002 increases R-loop accumulation

A, B) Competitive binding involved the initial treatment with NYH002 (2 μM) or DMSO for 1 hour, followed by the addition of NYH002P (1 μM) for an additional five hours. Click chemistry was performed between NYH002P and the AF647 fluorescent probe for immunofluorescence analysis in DLD1 cells, or alternatively with biotin for subsequent HRP-based detection in WCL by immunoblotting.

C) MS label-free quantification of gel-separated proteins was performed on NYH002P-biotin co-immunoprecipitation from DLD1 WCL. Direct (core) and indirect (accessory) drug–protein interactors were classified as either 'identified', which matched the expected molecular weight, or 'misidentified', which showed an incorrect molecular weight (n = 3).

D) NYH002P–protein interactome was curated using the nuclear complex dataset from CORUM followed by the construction of a PPI network with STRING.

E) Validation of NYH002-interacting proteins that were identified from the 'transcription' cluster in STRING. Co-immunoprecipitation was performed using click chemistry between NYH002P and biotin in DLD1 cells. Input represents 1% of the total WCL.

F) Competitive binding of NYH002P-interacting proteins was assessed by co-immunoprecipitation in DLD1 cells. Input represents 1% of the total WCL.

G) Direct visualization of drug–protein interactions. Proximity ligation assay (PLA) was carried out between the indicated proteins and post-treatment with NYH002P (1 μM) at six hours in DLD1 cells. PLA foci in the nucleus represent physical drug–protein interaction. LEF-1 nuclear protein was used as a negative control. Scale bar: 10μm

H) Cellular thermal shift assay was employed to determine the direct interaction between NYH002 and ILF2. DMSO was used as a negative control.

I) A simplified model based on AlphaFold3 prediction of the ILF2 protein complex.

J, K) Immunoblot of the ILF2 complex revealed that treatment with 1 μM NYH002 for 24 hours in DLD1 cells phenocopied the effect of ILF2 depletion by siRNA.

L, M, N) Phenotypic characterization of R-loops in siRNA-mediated ILF2-depleted DLD1 cells at 48 hours post-transfection. Loss of ILF2 resulted in the induction of S9.6, ssDNA, and γH2AX foci. Scale bar: 10μm.

O, P) Immunoblot showing downregulation of DHX9, WRN, and SETX helicases as a direct consequence of ILF2 targeting by NYH002 (1 μM, 24 hours post-treatment) or by siRNA-mediated depletion (48 hours post-transfection). GAPDH was used as a loading control.

Q) Co-immunoprecipitation of NYH002P-biotin via click chemistry revealed a direct interaction with ILF2 and DHX9, but neither with WRN nor SETX. Input represents 1% of the total WCL derived from DLD1 cells.

R) *In silico* STRING analysis indicated that the interaction of ILF2 with WRN and SETX is dependent on DHX9.

S) PLA in the nucleus of DLD1 cells showed direct interaction between ILF2 and DHX9 (n=3).
T) siRNA-mediated ILF2 depletion in DLD1 cells resulted in a significant reduction in PLA foci formation between NYH002P and DHX9 (n = 3).
Data are presented as mean ± SEM. Mann-Whitney U test without p value correction (A, L and M), two-way ANOVA (I and T) and unpaired two-tailed t-test (N). p values < 0.05 were considered significant.

**Figure 5:** NYH002 synergizes with DNA-damaging agents to suppress tumor progression and exhibits monotherapy efficacy against cancer cells with replication stress.
A) A series of dose–response matrices of NYH002 in combination with TMZ, 5-FU, or MMS. Synergy map showed the combination effects of DLD1 cell survival as indicated by SynergyFinder 3.0. A score of >10 indicates synergistic, <10 indicates additive, and <-10 indicates antagonistic.
B, C) Synergistic effect of NYH002 with TMZ, 5-FU, or MMS on the induction of DNA DSBs and apoptosis. DLD1 cells received 0.5 μM NYH002, 1.5 mM TMZ, 0.1 mM 5-FU, or 0.5 mM MMS as monotherapies or in combination, as indicated, for 24 hours prior to immunostaining for γH2AX. Alternatively, WCL were prepared for immunoblotting to examine cleaved caspase-3. Vinculin was used as a loading control.
D) Synergy of NYH002 and TMZ *in vivo*. Flank tumor implantation was performed by injecting 1 x $10^6$ cells into the subcutaneous space of the animals, followed by intraperitoneal dosing of NYH002 in combination with TMZ for nine weeks. Tumor growth was monitored and measured daily. A control cull was performed at day 63.
E, F) Immunoblot of differential protein expression of CCNE1 and E2F1 as indicators for $G_1$/S checkpoint deficiency. MCF7 and MDA-MB436 cell lines represent a matched tumor pair for breast cancer, whereas U251 and U2OS serve as a non-paired tumor comprising of glioblastoma and osteosarcoma, respectively. Vinculin was used as a loading control.
G, H) Baseline replication stress is indicated by the presence of unresolved γH2AX as shown by the different cell lines (n=3).
I, J) Increased susceptibility to replication-induced DSBs after treatment with 0.5 – 1.5 μM of NYH002 for 24 hours was observed in MDA-MB436 and U2OS cells with $G_1$/S-phase checkpoint deficiency, as compared to MCF7 and U251 cells with normal cell cycle progression (n=3).
K, L) $EC_{50}$ of NYH002 was determined after 48 hours in both paired-match (MCF7 and MDA-MB436) and non-paired (U251 and U2OS) cell lines (n=3).
Data are presented as mean ± SEM. Mann-Whitney U test without p value correction (B, G and H) and one-way ANOVA (I and J). p values < 0.05 were considered significant.

**Figure 6:** NYH002 therapy is lethal in HR deficient tumors.
A, B) Reproducibility of the siRNA DDR library screen for gene candidates (blue region). Spearman correlation was determined between the two independent replicates of Z-scores A and B in assessing the inhibition of DLD1 cell growth after 72 hours of treatment. The percentile ranking was based on the mean difference in growth inhibition between NYH002- and DMSO-treated DLD1 cells transduced with individual siRNA DDR gene candidates (n = 239).

C) STRING enrichment of the top 90th percentile of gene candidates identified in the DDR response category.

D) siRNA-mediated depletion of HR gene transcripts, identified in the top 90th percentile was assessed 48 hours post-transfection by immunoblotting with WCL of DLD1 cells.

E) Synergistic interaction between NYH002 and individual HR genes (EXO1, MSH3, and FEN1) was assessed based on cell survival readout at 72 hours post-treatment and calculated using the coefficient of drug interaction (CDI). Genomic scar scores were selected for nine HR-proficient and one HR-deficient cancer cell line, as indicated. CDI < 1 indicates synergistic (Syn), CDI = 1 indicates additive (Add), and CDI > 1 indicates antagonistic (Ant).

F) Dose response of NYH002 in the colony formation assay of HR-proficient (A549) and HR-deficient (NCI-H1299) cell lines after seven days of treatment (n=3).

G, H) Pharmacokinetics was determined by intraperitoneal administration of 25 mg/kg NYH002 in BALB/cJ mice, followed by a series of control cull at 2, 4, 8, 16, and 24 hours. Plasma and animal organs were processed and subsequently resuspended in acetonitrile solution to precipitate NYH002 for detection and quantification by MS.

I, J, K) Cytotoxicity of NYH002 was assessed by administering either DMSO or 25 mg/kg NYH002 via intraperitoneal injection into Nude mice on alternate days for two weeks, followed by a control cull to collect whole blood for hematologic viability analysis. The kidney and liver were also fixed and processed for H&E staining to assess changes in tissue architecture and the presence of necrotic cells

L, M) Assessment of NYH002 therapeutic efficacy in xenograft lung cancer models. Nude mice were randomly assigned and implanted with 1 x $10^6$ HR-proficient (A549) or HR-deficient (NCI-H1299) cells into the subcutaneous space of the animal's flank. Treatment was subsequently administered as either vehicle or 25 mg/kg NYH002 via intratumoral injection. Tumor size was measured alternate days for a period of two weeks. A control cull was performed upon completion of the treatment regimen.

N, O) Therapeutic assessment of NYH002 in orthotopic breast cancer models. Nude mice were randomly assigned and implanted with 1 x $10^6$ of HR proficient (MDA-MB231) and HR deficient (MDA-MB436) cells in the mammary fat pad. Treatment was subsequently administered as either vehicle or 25 mg/kg NYH002 via intraperitoneal injection. Tumor size was measured every alternate day for two weeks. A control cull was performed upon completion of the treatment regimen.

Data are presented as mean ± SEM. Unpaired two-tailed t-test (E and I) and two-way ANOVA (L, M, N and O). p values < 0.05 were considered significant whereas N.S was regarded as not significant.

**Figure 7**: A proposed model.

Therapeutic framework illustrating the mechanisms of action of NYH002. Created with BioRender.com.

**REFERENCE**


1. Hamperl S, Bocek MJ, Saldivar JC, Swigut T, Cimprich KA. Transcription-Replication Conflict Orientation Modulates R-Loop Levels and Activates Distinct DNA Damage Responses. Cell. 2017;170(4):774-86 e19.
2. Lam FC, Kong YW, Huang Q, Vu Han TL, Maffa AD, Kasper EM, et al. BRD4 prevents the accumulation of R-loops and protects against transcription-replication collision events and DNA damage. Nat Commun. 2020;11(1):4083.
3. Bayona-Feliu A, Herrera-Moyano E, Badra-Fajardo N, Galvan-Femenia I, Soler-Oliva ME, Aguilera A. The chromatin network helps prevent cancer-associated mutagenesis at transcription-replication conflicts. Nat Commun. 2023;14(1):6890.
4. Patel PS, Algouneh A, Krishnan R, Reynolds JJ, Nixon KCJ, Hao J, et al. Excessive transcription-replication conflicts are a vulnerability of BRCA1-mutant cancers. Nucleic Acids Res. 2023;51(9):4341-62.
5. Shinriki S, Hirayama M, Nagamachi A, Yokoyama A, Kawamura T, Kanai A, et al. DDX41 coordinates RNA splicing and transcriptional elongation to prevent DNA replication stress in hematopoietic cells. Leukemia. 2022;36(11):2605-20.
6. Gan W, Guan Z, Liu J, Gui T, Shen K, Manley JL, et al. R-loop-mediated genomic instability is caused by impairment of replication fork progression. Genes Dev. 2011;25(19):2041-56.
7. Tutt ANJ, Garber JE, Kaufman B, Viale G, Fumagalli D, Rastogi P, et al. Adjuvant Olaparib for Patients with BRCA1- or BRCA2-Mutated Breast Cancer. N Engl J Med. 2021;384(25):2394-405.
8. Yap TA, O'Carrigan B, Penney MS, Lim JS, Brown JS, Luken MJdM, et al. Phase I Trial of First-in-Class ATR Inhibitor M6620 (VX-970) as Monotherapy or in Combination With Carboplatin in Patients With Advanced Solid Tumors. J Clin Oncol. 2020;38:3195-204.
9. Patouret R, Cham N, Chiba S. Collective Synthesis of Highly Oxygenated (Furano)germacranolides Derived from Elephantopus mollis and Elephantopus tomentosus. Angew Chem Int Ed Engl. 2024;63(19):e202402050.
10. Jung Y, Kraikivski P, Shafiekhani S, Terhune SS, Dash RK. Crosstalk between Plk1, p53, cell cycle, and G2/M DNA damage checkpoint regulation in cancer: computational modeling and analysis. NPJ Syst Biol Appl. 2021;7(1):46.
11. Leriche M, Bonnet C, Jana J, Chhetri G, Mennour S, Martineau S, et al. 53BP1 interacts with the RNA primer from Okazaki fragments to support their processing during unperturbed DNA replication. Cell Rep. 2023;42(11):113412.
12. Lukas C, Savic V, Bekker-Jensen S, Doil C, Neumann B, Pedersen RS, et al. 53BP1 nuclear bodies form around DNA lesions generated by mitotic transmission of chromosomes under replication stress. Nat Cell Biol. 2011;13(3):243-53.
13. Einig E, Jin C, Andrioletti V, Macek B, Popov N. RNAPII-dependent ATM signaling at collisions with replication forks. Nat Commun. 2023;14(1):5147.
14. Awwad SW, Doyle C, Coulthard J, Bader AS, Gueorguieva N, Lam S, et al. KLF5 loss sensitizes cells to ATR inhibition and is synthetic lethal with ARID1A deficiency. Nat Commun. 2025;16(1):480.

15. Tsitsiridis G, Steinkamp R, Giurgiu M, Brauner B, Fobo G, Frishman G, et al. CORUM: the comprehensive resource of mammalian protein complexes-2022. Nucleic Acids Res. 2023;51(D1):D539-D45.
16. Jafari R, Almqvist H, Axelsson H, Ignatushchenko M, Lundback T, Nordlund P, et al. The cellular thermal shift assay for evaluating drug target interactions in cells. Nat Protoc. 2014;9(9):2100-22.
17. Chiu CL, Li CG, Verschueren E, Wen RM, Zhang D, Gordon CA, et al. NUSAP1 Binds ILF2 to Modulate R-Loop Accumulation and DNA Damage in Prostate Cancer. Int J Mol Sci. 2023;24(7).
18. Marabitti V, Lillo G, Malacaria E, Palermo V, Sanchez M, Pichierri P, et al. ATM pathway activation limits R-loop-associated genomic instability in Werner syndrome cells. Nucleic Acids Res. 2019;47(7):3485-502.
19. Rao S, Andrs M, Shukla K, Isik E, Konig C, Schneider S, et al. Senataxin RNA/DNA helicase promotes replication restart at co-transcriptional R-loops to prevent MUS81-dependent fork degradation. Nucleic Acids Res. 2024;52(17):10355-69.
20. Kitange GJ, Mladek AC, Schroeder MA, Pokorny JC, Carlson BL, Zhang Y, et al. Retinoblastoma Binding Protein 4 Modulates Temozolomide Sensitivity in Glioblastoma by Regulating DNA Repair Proteins. Cell Rep. 2016;14(11):2587-98.
21. Martino-Echarri E, Henderson BR, Brocardo MG. Targeting the DNA replication checkpoint by pharmacologic inhibition of Chk1 kinase: a strategy to sensitize APC mutant colon cancer cells to 5-fluorouracil chemotherapy. Oncotarget. 2014;5:9889-900.
22. Kok YP, Guerrero Llobet S, Schoonen PM, Everts M, Bhattacharya A, Fehrmann RSN, et al. Overexpression of Cyclin E1 or Cdc25A leads to replication stress, mitotic aberrancies, and increased sensitivity to replication checkpoint inhibitors. Oncogenesis. 2020;9(10):88.
23. Khanna KK, Keating KE, Kozlov S, Scott S, Gatei M, Hobson K, et al. ATM associates with and phosphorylates p53: mapping the region of interaction. Nat Gen. 1998;20:398-400.
24. Guo E, Ishii Y, Mueller J, Srivatsan A, Gahman T, Putnam CD, et al. FEN1 endonuclease as a therapeutic target for human cancers with defects in homologous recombination. Proc Natl Acad Sci U S A. 2020;117(32):19415-24.
25. Li Y, Zhang Y, Shah SB, Chang CY, Wang H, Wu X. MutSbeta protects common fragile sites by facilitating homology-directed repair at DNA double-strand breaks with secondary structures. Nucleic Acids Res. 2024;52(3):1120-35.
26. van de Kooij B, Schreuder A, Pavani R, Garzero V, Uruci S, Wendel TJ, et al. EXO1 protects BRCA1-deficient cells against toxic DNA lesions. Mol Cell. 2024;84(4):659-74 e7.
27. Nguyen L, J WMM, Van Hoeck A, Cuppen E. Pan-cancer landscape of homologous recombination deficiency. Nat Commun. 2020;11(1):5584.
28. Barretina J, Caponigro G, Stransky N, Venkatesan K, Margolin AA, Kim S, et al. The Cancer Cell Line Encyclopedia enables predictive modelling of anticancer drug sensitivity. Nature. 2012;483(7391):603-7.
29. Rempel E, Kluck K, Beck S, Ourailidis I, Kazdal D, Neumann O, et al. Pan-cancer analysis of genomic scar patterns caused by homologous repair deficiency (HRD). NPJ Precis Oncol. 2022;6(1):36.

30. Wu D, Chen Q, Chen X, Han F, Chen Z, Wang Y. The blood-brain barrier: structure, regulation, and drug delivery. Signal Transduct Target Ther. 2023;8(1):217.
31. Garcia-Muse T, Aguilera A. R Loops: From Physiological to Pathological Roles. Cell. 2019;179(3):604-18.
32. Chakraborty P, Grosse F. Human DHX9 helicase preferentially unwinds RNA-containing displacement loops (R-loops) and G-quadruplexes. DNA Repair. 2011;10(6):654-65.
33. Chakraborty P, Huang JTJ, Hiom K. DHX9 helicase promotes R-loop formation in cells with impaired RNA splicing. Nat Commun. 2018;9(1):4346.
34. Yang BZ, Liu MY, Chiu KL, Chien YL, Cheng CA, Chen YL, et al. DHX9 SUMOylation is required for the suppression of R-loop-associated genome instability. Nat Commun. 2024;15(1):6009.
35. Zardoni L, Nardini E, Brambati A, Lucca C, Choudhary R, Loperfido F, et al. Elongating RNA polymerase II and RNA:DNA hybrids hinder fork progression and gene expression at sites of head-on replication-transcription collisions. Nucleic Acids Res. 2021;49(22):12769-84.
36. Skourti-Stathaki K, Proudfoot NJ, Gromak N. Human senataxin resolves RNA/DNA hybrids formed at transcriptional pause sites to promote Xrn2-dependent termination. Mol Cell. 2011;42(6):794-805.
37. Noto A, Valenzisi P, Di Feo F, Fratini F, Kulikowicz T, Sommers JA, et al. Phosphorylation-dependent WRN-RPA interaction promotes recovery of stalled forks at secondary DNA structure. Nat Commun. 2025;16(1):997.
38. Polenkowski M, Allister AB, Burbano de Lara S, Pierce A, Geary B, El Bounkari O, et al. THOC5 complexes with DDX5, DDX17, and CDK12 to regulate R loop structures and transcription elongation rate. iScience. 2023;26(1):105784.
39. Secchi M, Garbelli A, Riva V, Deidda G, Santonicola C, Formica TM, et al. Synergistic action of human RNaseH2 and the RNA helicase-nuclease DDX3X in processing R-loops. Nucleic Acids Res. 2024;52(19):11641-58.
40. Yu Z, Mersaoui SY, Guitton-Sert L, Coulombe Y, Song J, Masson JY, et al. DDX5 resolves R-loops at DNA double-strand breaks to promote DNA repair and avoid chromosomal deletions. NAR Cancer. 2020;2(3):zcaa028.
41. Uhlen M, Fagerberg L, Hallstrom BM, Lindskog C, Oksvold P, Mardinoglu A, et al. Proteomics. Tissue-based map of the human proteome. Science. 2015;347(6220):1260419.
42. Kazuma Y, Shirakawa K, Tashiro Y, Yamazaki H, Nomura R, Horisawa Y, et al. ILF2 enhances the DNA cytosine deaminase activity of tumor mutator APOBEC3B in multiple myeloma cells. Sci Rep. 2022;12(1):2278.
43. Ling Z, Pan J, Zhang Z, Chen G, Geng J, Lin Q, et al. Small-molecule Molephantin induces apoptosis and mitophagy flux blockage through ROS production in glioblastoma. Cancer Lett. 2024;592:216927.
44. Krishnan R, Lapierre M, Gautreau B, Nixon KCJ, El Ghamrasni S, Patel PS, et al. RNF8 ubiquitylation of XRN2 facilitates R-loop resolution and restrains genomic instability in BRCA1 mutant cells. Nucleic Acids Res. 2023;51(19):10484-505.

45. Ciriello G, Miller ML, Aksoy BA, Senbabaoglu Y, Schultz N, Sander C. Emerging landscape of oncogenic signatures across human cancers. Nat Genet. 2013;45(10):1127-33.
46. Ianevski A, Giri AK, Aittokallio T. SynergyFinder 3.0: an interactive analysis and consensus interpretation of multi-drug synergies across multiple samples. Nucleic Acids Res. 2022;50(W1):W739-W43.
47. Kim H, Xu H, George E, Hallberg D, Kumar S, Jagannathan V, et al. Combining PARP with ATR inhibition overcomes PARP inhibitor and platinum resistance in ovarian cancer models. Nat Commun. 2020;11(1):3726.
48. Lim YC, Ensbey KS, Offenhauser C, D'Souza R CJ, Cullen JK, Stringer BW, et al. Simultaneous targeting of DNA replication and homologous recombination in glioblastoma with a polyether ionophore. Neuro Oncol. 2020;22(2):216-28.
49. Maya-Mendoza A, Moudry P, Merchut-Maya JM, Lee M, Strauss R, Bartek J. High speed of fork progression induces DNA replication stress and genomic instability. Nature. 2018;559(7713):279-84.
50. Bindea G, Mlecnik B, Hackl H, Charoentong P, Tosolini M, Kirilovsky A, et al. ClueGO: a Cytoscape plug-in to decipher functionally grouped gene ontology and pathway annotation networks. Bioinformatics. 2009;25(8):1091-3.
51. Abdennur N, Mirny LA. Cooler: scalable storage for Hi-C data and other genomically labeled arrays. Bioinformatics. 2020;36(1):311-6.
52. Flyamer IM, Illingworth RS, Bickmore WA. Coolpup.py: versatile pile-up analysis of Hi-C data. Bioinformatics. 2020;36(10):2980-5.
53. Wolff J, Rabbani L, Gilsbach R, Richard G, Manke T, Backofen R, et al. Galaxy HiCExplorer 3: a web server for reproducible Hi-C, capture Hi-C and single-cell Hi-C data analysis, quality control and visualization. Nucleic Acids Res. 2020;48(W1):W177-W84.

**Figure 1**

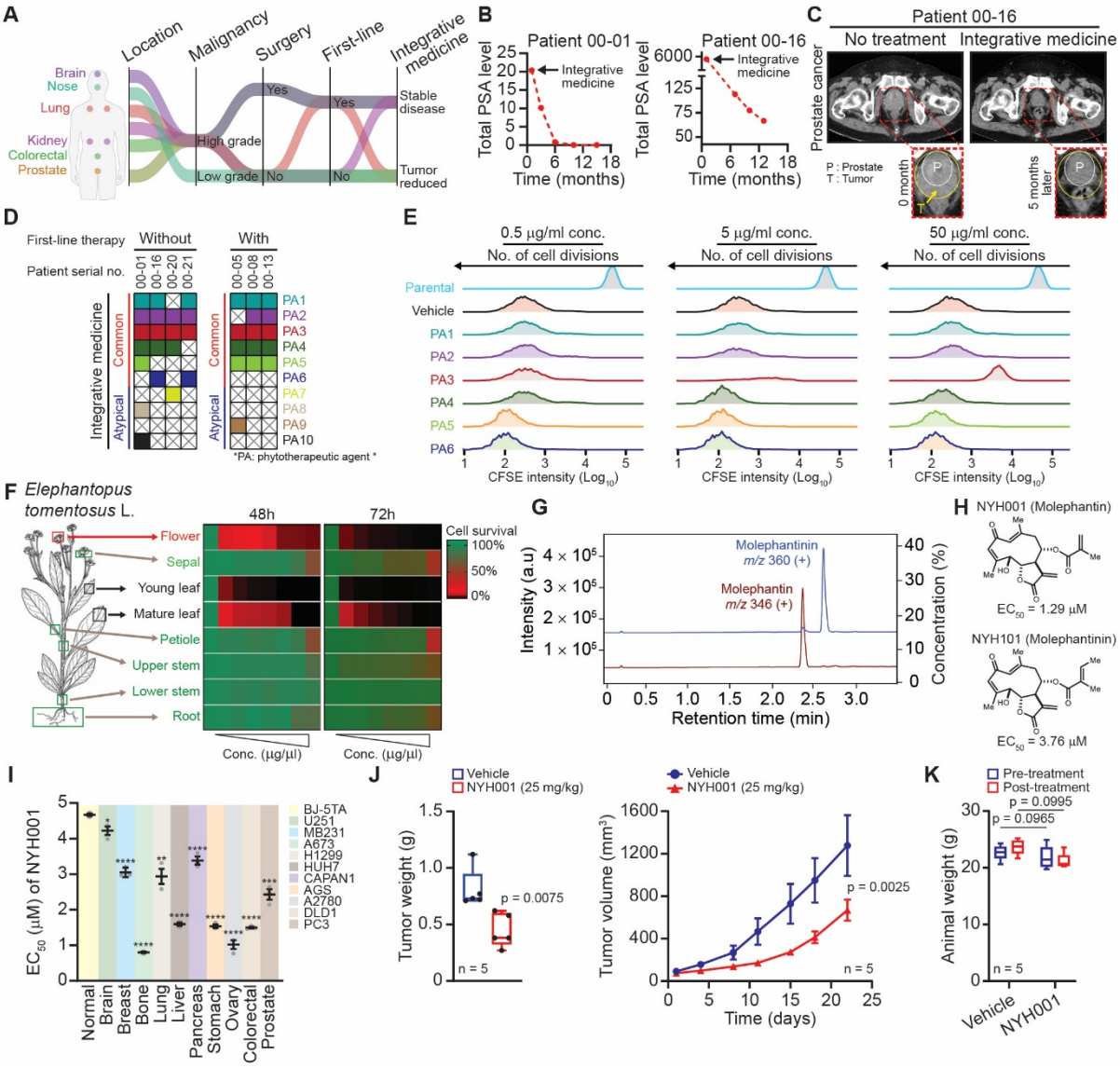
A
Location
Malignancy
Surgery
First-line
Integrative medicine
Brain
Nose
Lung
Kidney
Colorectal
Prostate
Yes
High grade
Low grade
No
Stable disease
Tumor reduced
B
Patient 00-01
Patient 00-16
Total PSA level
Integrative medicine
Time (months)
C
Patient 00-16
No treatment
Integrative medicine
Prostate cancer
P : Prostate
T : Tumor
0 month
5 months later
D
First-line therapy
Without
With
Patient serial no.
00-01
00-16
00-20
00-21
00-05
00-08
00-13
Integrative medicine
Common
Atypical
PA1
PA2
PA3
PA4
PA5
PA6
PA7
PA8
PA9
PA10
*PA: phytotherapeutic agent *
E
0.5 μg/ml conc.
5 μg/ml conc.
50 μg/ml conc.
No. of cell divisions
Parental
Vehicle
CFSE intensity (Log10)
F
Elephantopus tomentosus L.
48h
72h
Flower
Sepal
Young leaf
Mature leaf
Petiole
Upper stem
Lower stem
Root
Cell survival
100%
50%
0%
Conc. (μg/μl)
G
Molephantinin
m/z 360 (+)
Molephantin
m/z 346 (+)
Intensity (a.u)
Concentration (%)
Retention time (min)
H
NYH001 (Molephantin)
EC50 = 1.29 μM
NYH101 (Molephantinin)
EC50 = 3.76 μM
I
EC50 (μM) of NYH001
BJ-5TA
U251
MB231
A673
H1299
HUH7
CAPAN1
AGS
A2780
DLD1
PC3
Normal
Brain
Breast
Bone
Lung
Liver
Pancreas
Stomach
Ovary
Colorectal
Prostate
J
Vehicle
NYH001 (25 mg/kg)
Tumor weight (g)
p = 0.0075
n = 5
Tumor volume (mm3)
p = 0.0025
Time (days)
K
Pre-treatment
Post-treatment
p = 0.0995
p = 0.0965
Animal weight (g)
Vehicle
NYH001

Figure 2

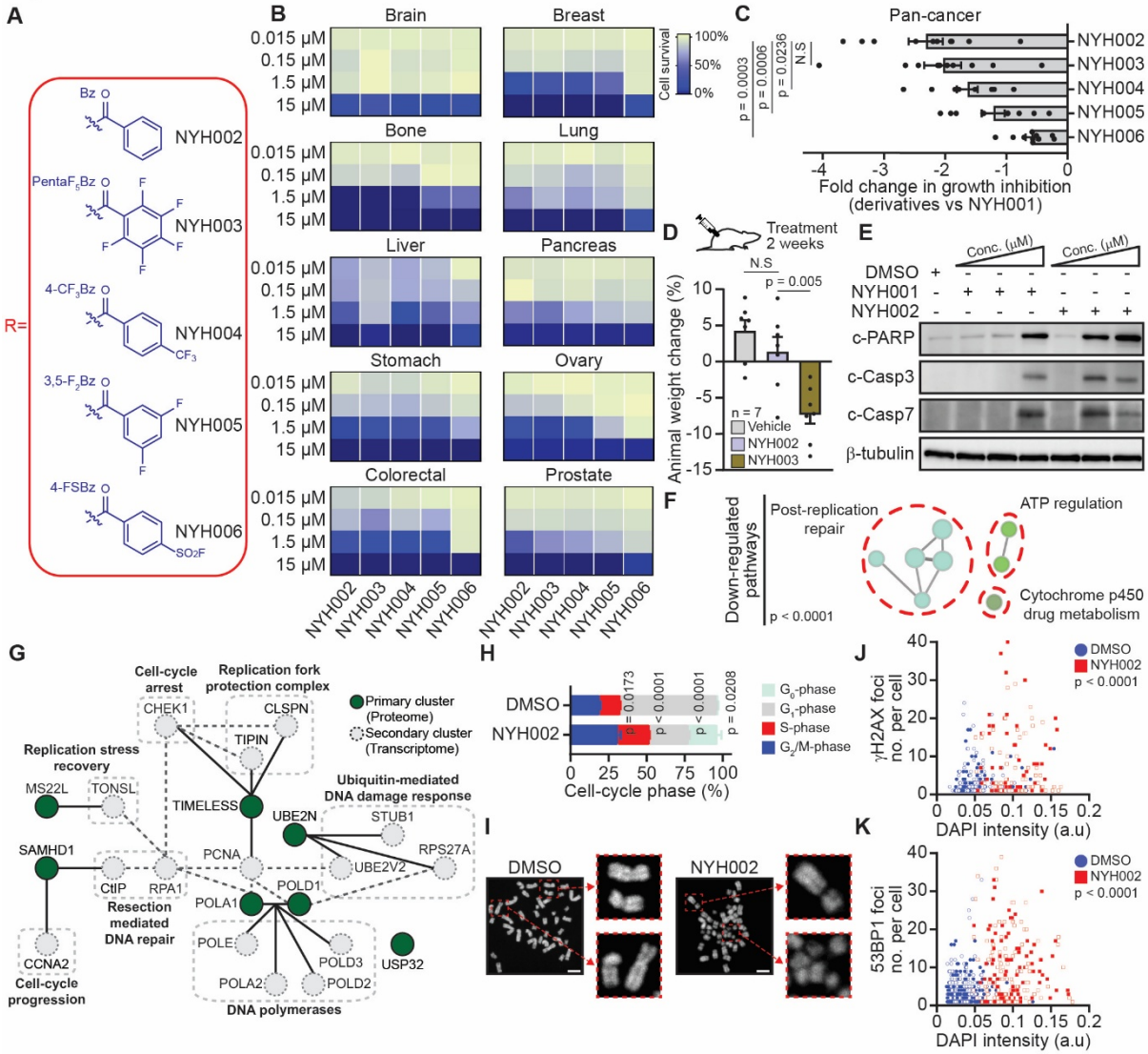
A
R=
Bz
NYH002
PentaF5Bz
NYH003
4-CF3Bz
NYH004
3,5-F2Bz
NYH005
4-FSBz
NYH006
B
Brain
Breast
Bone
Lung
Liver
Pancreas
Stomach
Ovary
Colorectal
Prostate
0.015 μM
0.15 μM
1.5 μM
15 μM
Cell survival
100%
50%
0%
C
Pan-cancer
p = 0.0003
p = 0.0006
p = 0.0236
N.S
Fold change in growth inhibition
(derivatives vs NYH001)
D
Treatment
2 weeks
N.S
p = 0.005
Animal weight change (%)
n = 7
Vehicle
NYH002
NYH003
E
Conc. (μM)
DMSO
NYH001
NYH002
c-PARP
c-Casp3
c-Casp7
β-tubulin
F
Down-regulated pathways
Post-replication repair
p < 0.0001
ATP regulation
Cytochrome p450 drug metabolism
G
Cell-cycle arrest
Replication fork protection complex
CHEK1
CLSPN
TIPIN
Primary cluster (Proteome)
Secondary cluster (Transcriptome)
Replication stress recovery
MS22L
TONSL
TIMELESS
Ubiquitin-mediated DNA damage response
UBE2N
STUB1
RPS27A
UBE2V2
SAMHD1
PCNA
CtIP
RPA1
POLD1
POLA1
Resection mediated DNA repair
POLE
POLD3
USP32
CCNA2
Cell-cycle progression
POLA2
POLD2
DNA polymerases
H
DMSO
NYH002
p = 0.0173
p < 0.0001
p < 0.0001
p = 0.0208
G0-phase
G1-phase
S-phase
G2/M-phase
Cell-cycle phase (%)
I
DMSO
NYH002
J
γH2AX foci no. per cell
DAPI intensity (a.u)
p < 0.0001
K
53BP1 foci no. per cell
DAPI intensity (a.u)
p < 0.0001

Figure 3

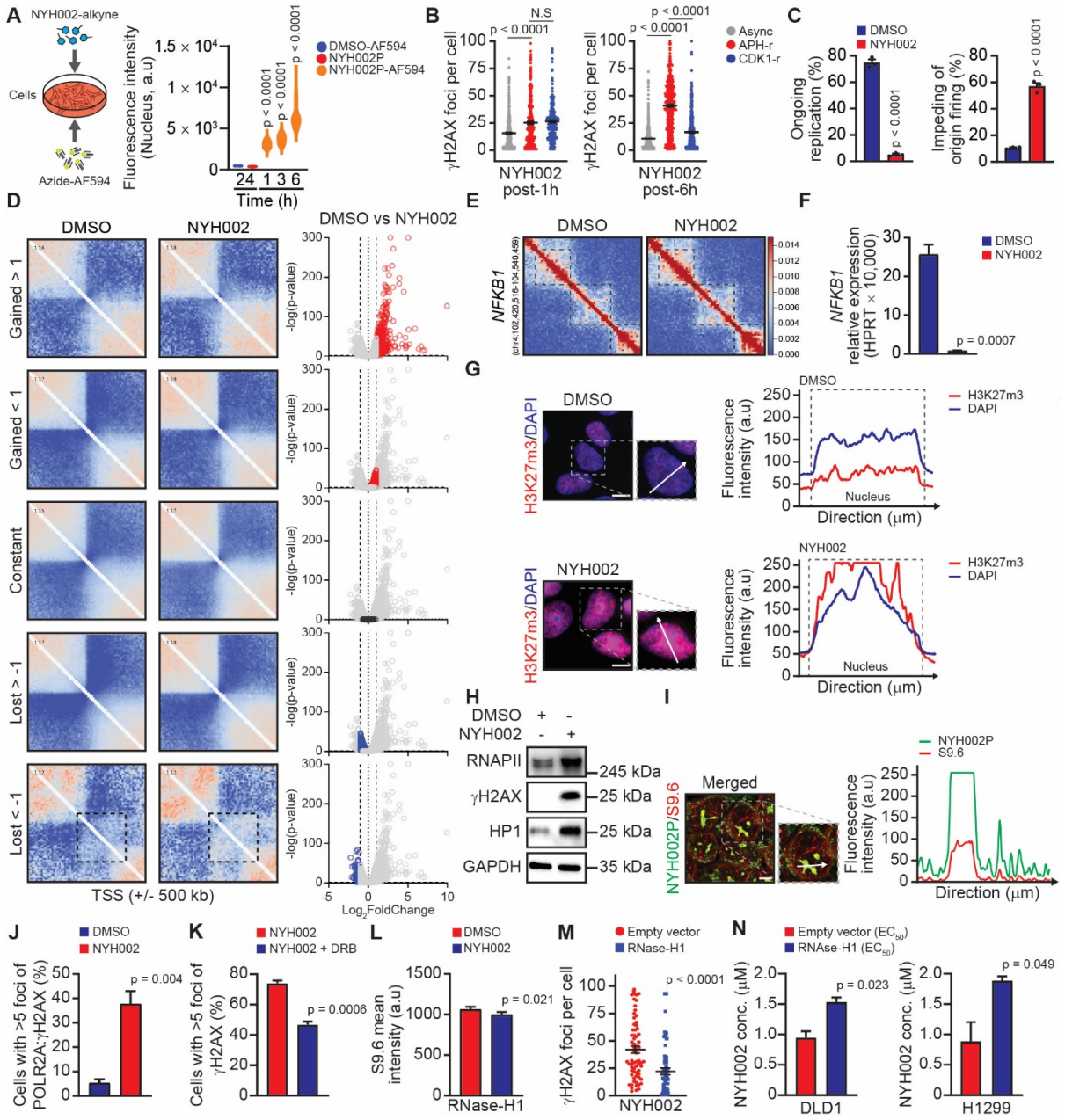
A
NYH002-alkyne
Cells
Azide-AF594
Fluorescence intensity (Nucleus, a.u)
DMSO-AF594
NYH002P
NYH002P-AF594
Time (h)
B
γH2AX foci per cell
NYH002 post-1h
NYH002 post-6h
Async
APH-r
CDK1-r
C
DMSO
NYH002
Ongoing replication (%)
Impeding of origin firing (%)
D
DMSO
NYH002
DMSO vs NYH002
Gained > 1
Gained < 1
Constant
Lost > -1
Lost < -1
-log(p-value)
TSS (+/- 500 kb)
Log2FoldChange
E
NFKB1
F
NFKB1 relative expression (HPRT × 10,000)
p = 0.0007
G
H3K27m3/DAPI
Fluorescence intensity (a.u)
Nucleus
Direction (μm)
H
RNAPII
γH2AX
HP1
GAPDH
245 kDa
25 kDa
35 kDa
I
Merged
NYH002P/S9.6
J
Cells with >5 foci of POLR2A:γH2AX (%)
p = 0.004
K
Cells with >5 foci of γH2AX (%)
NYH002 + DRB
p = 0.0006
L
S9.6 mean intensity (a.u)
RNase-H1
p = 0.021
M
Empty vector
RNase-H1
p < 0.0001
N
Empty vector (EC50)
RNAse-H1 (EC50)
NYH002 conc. (μM)
DLD1
H1299
p = 0.023
p = 0.049

**Figure 4**

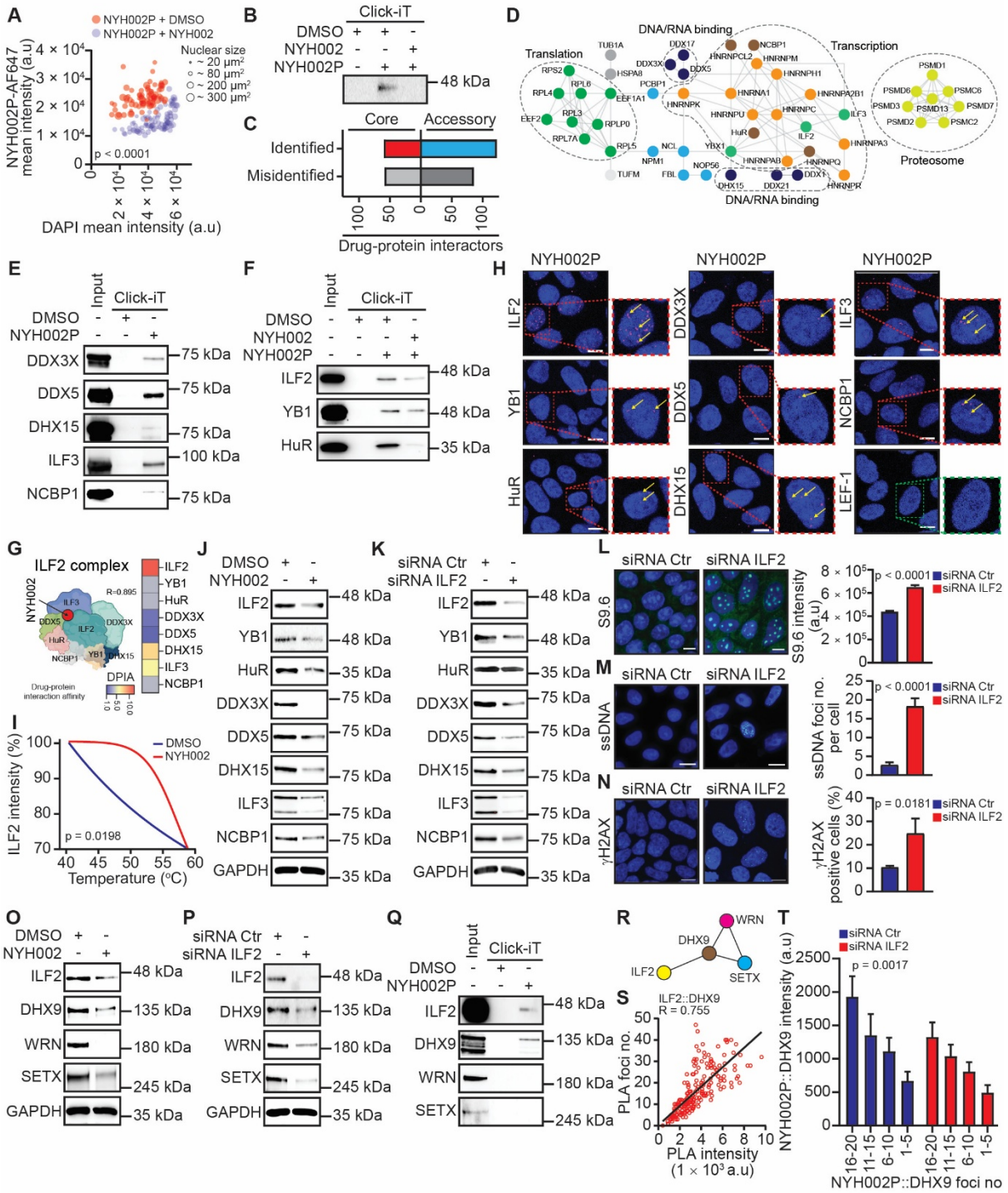
A
NYH002P + DMSO
NYH002P + NYH002
Nuclear size
~ 20 µm²
~ 80 µm²
~ 200 µm²
~ 300 µm²
NYH002P-AF647 mean intensity (a.u)
p < 0.0001
DAPI mean intensity (a.u)
B
Click-iT
DMSO
NYH002
NYH002P
48 kDa
C
Core
Accessory
Identified
Misidentified
Drug-protein interactors
D
DNA/RNA binding
Translation
Transcription
Proteosome
E
Input
Click-iT
DDX3X
DDX5
DHX15
ILF3
NCBP1
75 kDa
100 kDa
F
ILF2
YB1
HuR
48 kDa
35 kDa
H
NYH002P
ILF2
DDX3X
ILF3
YB1
DDX5
NCBP1
HuR
DHX15
LEF-1
G
ILF2 complex
NYH002
R=0.895
DPIA
Drug-protein interaction affinity
I
ILF2 intensity (%)
DMSO
NYH002
p = 0.0198
Temperature (°C)
J
K
siRNA Ctr
siRNA ILF2
GAPDH
L
S9.6
S9.6 intensity (a.u)
p < 0.0001
M
ssDNA
ssDNA foci no. per cell
N
γH2AX
γH2AX positive cells (%)
p = 0.0181
O
P
Q
R
WRN
DHX9
ILF2
SETX
S
ILF2::DHX9
R = 0.755
PLA foci no.
PLA intensity (1 × 10³ a.u)
T
p = 0.0017
NYH002P::DHX9 intensity (a.u)
NYH002P::DHX9 foci no

**Figure 5**

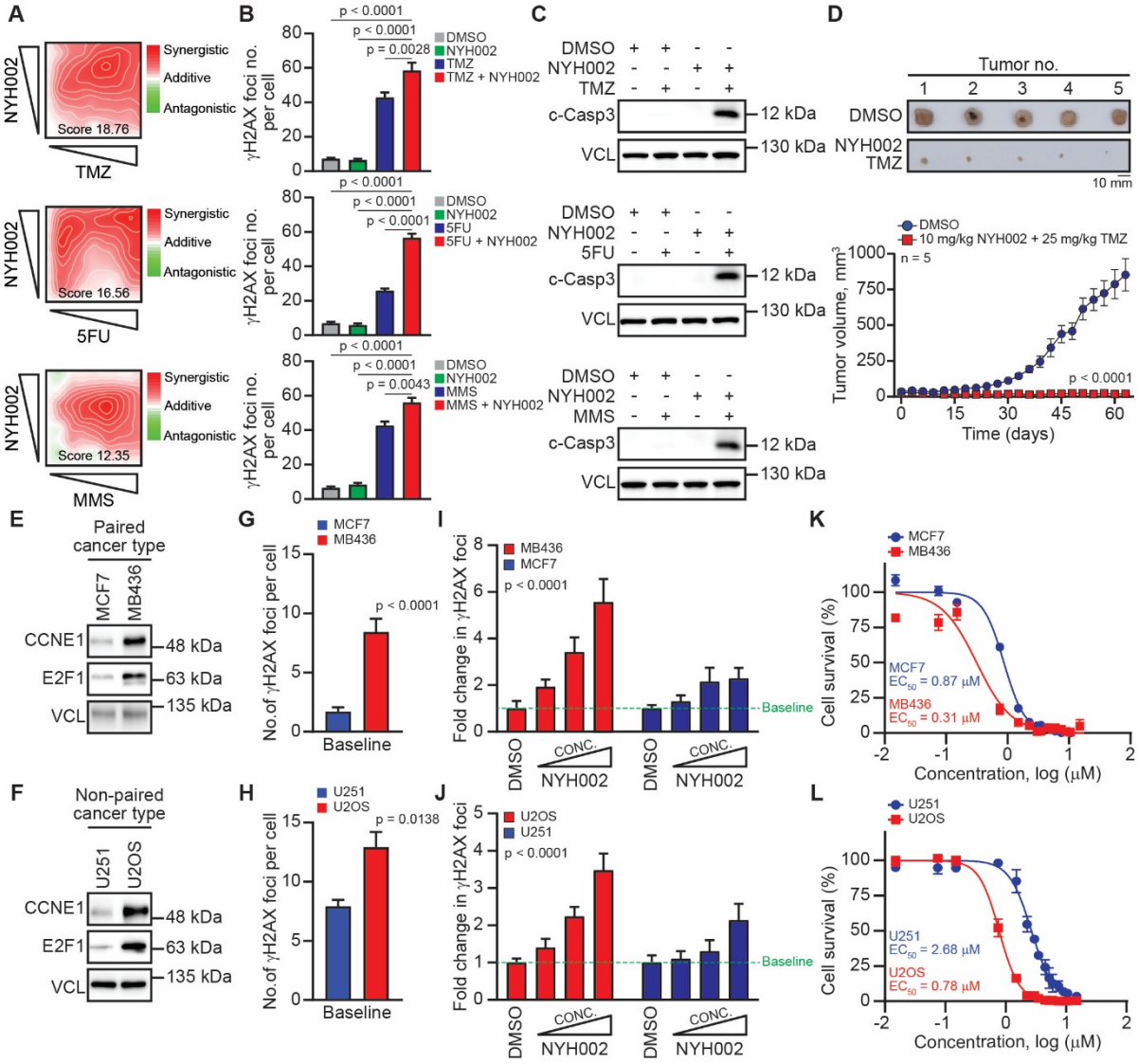
A
NYH002
TMZ
Score 18.76
Synergistic
Additive
Antagonistic
5FU
Score 16.56
MMS
Score 12.35
B
γH2AX foci no. per cell
p < 0.0001
p = 0.0028
p = 0.0043
DMSO
NYH002
TMZ
TMZ + NYH002
5FU
5FU + NYH002
MMS
MMS + NYH002
C
DMSO
NYH002
TMZ
5FU
MMS
c-Casp3
VCL
12 kDa
130 kDa
D
Tumor no.
1 2 3 4 5
DMSO
NYH002
TMZ
10 mm
10 mg/kg NYH002 + 25 mg/kg TMZ
n = 5
Tumor volume, mm³
Time (days)
p < 0.0001
E
Paired cancer type
MCF7
MB436
CCNE1
E2F1
VCL
48 kDa
63 kDa
135 kDa
G
No.of γH2AX foci per cell
Baseline
I
Fold change in γH2AX foci
CONC.
NYH002
K
Cell survival (%)
Concentration, log (μM)
MCF7
EC50 = 0.87 μM
MB436
EC50 = 0.31 μM
F
Non-paired cancer type
U251
U2OS
H
p = 0.0138
J
L
EC50 = 2.68 μM
EC50 = 0.78 μM

Figure 6

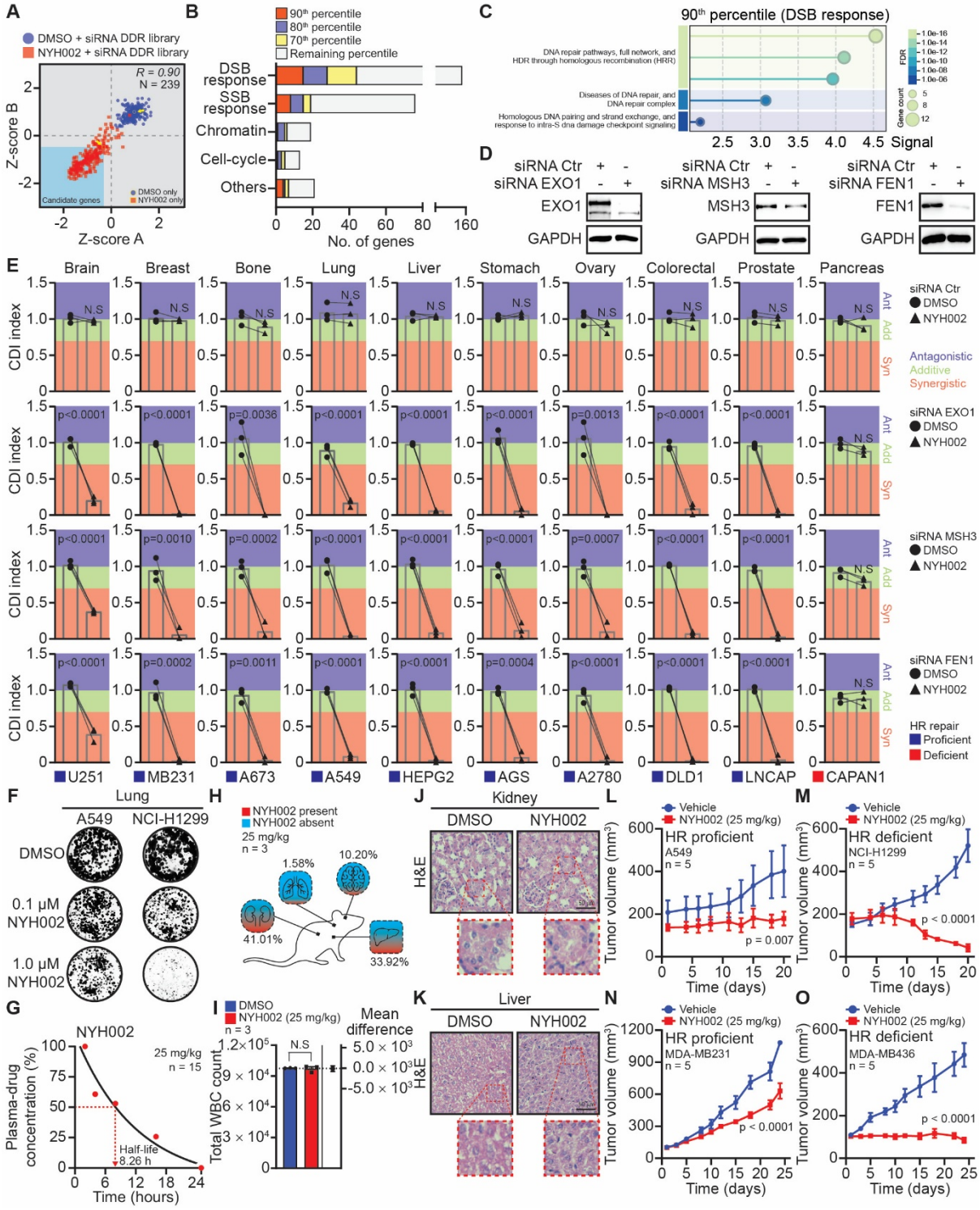
A
DMSO + siRNA DDR library
NYH002 + siRNA DDR library
R = 0.90
N = 239
Z-score B
Z-score A
Candidate genes
DMSO only
NYH002 only
B
90th percentile
80th percentile
70th percentile
Remaining percentile
DSB response
SSB response
Chromatin
Cell-cycle
Others
No. of genes
C
90th percentile (DSB response)
DNA repair pathways, full network, and HDR through homologous recombination (HRR)
Diseases of DNA repair, and DNA repair complex
Homologous DNA pairing and strand exchange, and response to intra-S dna damage checkpoint signaling
FDR
Gene count
Signal
D
siRNA Ctr
siRNA EXO1
siRNA MSH3
siRNA FEN1
EXO1
MSH3
FEN1
GAPDH
E
Brain
Breast
Bone
Lung
Liver
Stomach
Ovary
Colorectal
Prostate
Pancreas
CDI index
N.S
siRNA Ctr
siRNA EXO1
siRNA MSH3
siRNA FEN1
DMSO
NYH002
Ant
Add
Syn
Antagonistic
Additive
Synergistic
HR repair
Proficient
Deficient
U251
MB231
A673
A549
HEPG2
AGS
A2780
DLD1
LNCAP
CAPAN1
F
Lung
A549
NCI-H1299
DMSO
0.1 μM NYH002
1.0 μM NYH002
G
NYH002
25 mg/kg
n = 15
Plasma-drug concentration (%)
Half-life
8.26 h
Time (hours)
H
NYH002 present
NYH002 absent
25 mg/kg
n = 3
1.58%
10.20%
41.01%
33.92%
I
DMSO
NYH002 (25 mg/kg)
n = 3
N.S
Total WBC count
Mean difference
J
Kidney
DMSO
NYH002
H&E
K
Liver
DMSO
NYH002
H&E
L
Vehicle
NYH002 (25 mg/kg)
HR proficient
A549
n = 5
p = 0.007
Tumor volume (mm³)
Time (days)
M
Vehicle
NYH002 (25 mg/kg)
HR deficient
NCI-H1299
n = 5
p < 0.0001
Tumor volume (mm³)
Time (days)
N
Vehicle
NYH002 (25 mg/kg)
HR proficient
MDA-MB231
n = 5
p < 0.0001
Tumor volume (mm³)
Time (days)
O
Vehicle
NYH002 (25 mg/kg)
HR deficient
MDA-MB436
n = 5
p < 0.0001
Tumor volume (mm³)
Time (days)

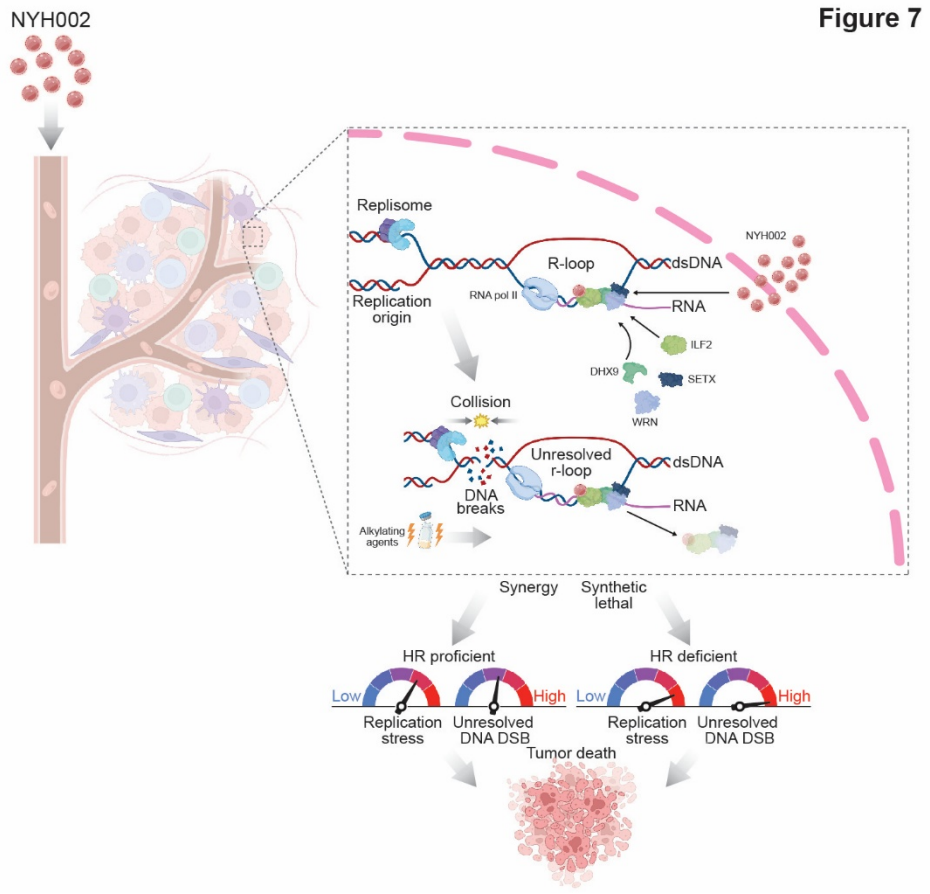
NYH002
Figure 7
Replisome
R-loop
dsDNA
NYH002
Replication origin
RNA pol II
RNA
ILF2
DHX9
SETX
WRN
Collision
Unresolved r-loop
dsDNA
DNA breaks
RNA
Alkylating agents
Synergy
Synthetic lethal
HR proficient
HR deficient
Low
High
Low
High
Replication stress
Unresolved DNA DSB
Replication stress
Unresolved DNA DSB
Tumor death